Geoscience Frontiers 11 (2020) 243–263

HOSTED BY

Contents lists available at ScienceDirect

China University of Geosciences (Beijing)

Geoscience Frontiers

journal homepage: www.elsevier.com/locate/gsf

Research Paper

High-precision geochronology of Mesozoic magmatism in Macao, Southeast China: Evidence for multistage granite emplacement

Pedro Quelhas [a,b], Ágata Alveirinho Dias [a,b,*], João Mata [a], Donald Wayne Davis [c], Maria Luísa Ribeiro [d]

[a] Institute of Science and Environment, University of Saint Joseph, Macao, China
[b] Instituto Dom Luiz, Faculdade de Ciências, Universidade de Lisboa, Lisboa, Portugal
[c] Jack Satterly Geochronology Laboratory, Department of Earth Sciences, University of Toronto, Toronto, Ont, Canada
[d] Laboratório Nacional de Engenharia e Geologia, Lisboa, Portugal

ARTICLE INFO

Article history:
Received 7 November 2018
Received in revised form
6 March 2019
Accepted 28 April 2019
Available online 25 May 2019
Handling Editor: Christopher J Spencer

Keywords:
Granites
U–Pb geochronology
Zircon
Jurassic
Yanshanian orogeny
Macao

ABSTRACT

Six new high precision U–Pb zircon ID-TIMS ages plus thirteen in situ high spatial resolution U–Pb zircon LA-MC-ICPMS ages are reported from Jurassic plutonic (metaluminous to weakly peraluminous biotite granites) and Jurassic to Cretaceous hypabyssal (dacites) rocks from Macao. Despite its relatively small area (~30 km^2), the new ages tightly constrain the Macao granitic magmatism to two periods ranging from 164.5 ± 0.6 Ma to 162.9 ± 0.7 Ma and 156.6 ± 0.2 Ma to 155.5 ± 0.8 Ma, separated by ca. 6 Ma. Inherited zircons point to the existence of a basement with ages up to Paleo-Proterozoic and late Archean in the region. In addition, younger dacitic rocks were dated at 150.6 ± 0.6 Ma and <120 Ma. U–Pb zircon ages and whole-rock REE data of Macao granites indicate that the first pulse is also represented in Hong Kong and Southeast (SE) China, while magmatism with the chemical characteristics of the second pulse seems to not be represented outside Macao. The two granitic magmatic pulses have distinct mineralogical and geochemical features that support their discrete nature rather than a continuum of comagmatic activity and suggest that the Macao granitic suite was incrementally assembled during a period of ca. 9 Ma, a hypothesis also extendable to the neighboring Hong Kong region for a time lapse of ca. 24 Ma. In Macao, the transition from granitic magmatism (Middle to Upper Jurassic) to the younger dacite dykes (Upper Jurassic to Lower Cretaceous) most likely corresponds to a change in the regional tectonic setting, from an extensional regime related with foundering of the subducting paleo-Pacific plate during the Early Yanshanian period to the reestablishment of a normal subduction system in SE China during the Late Yanshanian period.

1. Introduction

Granitic rocks are a major component of the upper continental crust, which has an estimated "granitic" average composition (e.g., Rudnick and Gao, 2003). Slight distinctive differences in their mineralogy and chemical composition have potential implications for their origin, which is crucial to understand the tectono-thermal evolution of continents (Kemp and Hawkesworth, 2003; Arndt, 2013).

Mesozoic granitic rocks are widely distributed in the Cathaysia Block, Southeast (SE) China. Along the coast of SE China, where Macao and Hong Kong are located, magmatism associated with the Yanshanian orogeny occurred in two main stages: Early Yanshanian (180–142 Ma) and Late Yanshanian (142–67 Ma; Zhou et al., 2006). In adjacent areas of Macao, different types of granites (I, S and A) occur with dominant Jurassic to Cretaceous ages (e.g., Li et al., 2007; Chen et al., 2012; Huang et al., 2013, 2015; Li et al., 2015; Zhang et al., 2015, 2017; Zhou et al., 2016; Qiu et al., 2017; Zheng et al., 2017a, b). However, many of these studies dealt with large batholith areas where sampling cannot adequately represent the small-scale compositional variation of plutonic bodies. Thus, detailed geochemical and age variation information can have been missed, which may have potentially important implications for the

* Corresponding author. Institute of Science and Environment, University of Saint Joseph, Macao, China.
E-mail address: agata.dias@usj.edu.mo (Á.A. Dias).
Peer-review under responsibility of China University of Geosciences (Beijing).

https://doi.org/10.1016/j.gsf.2019.04.011

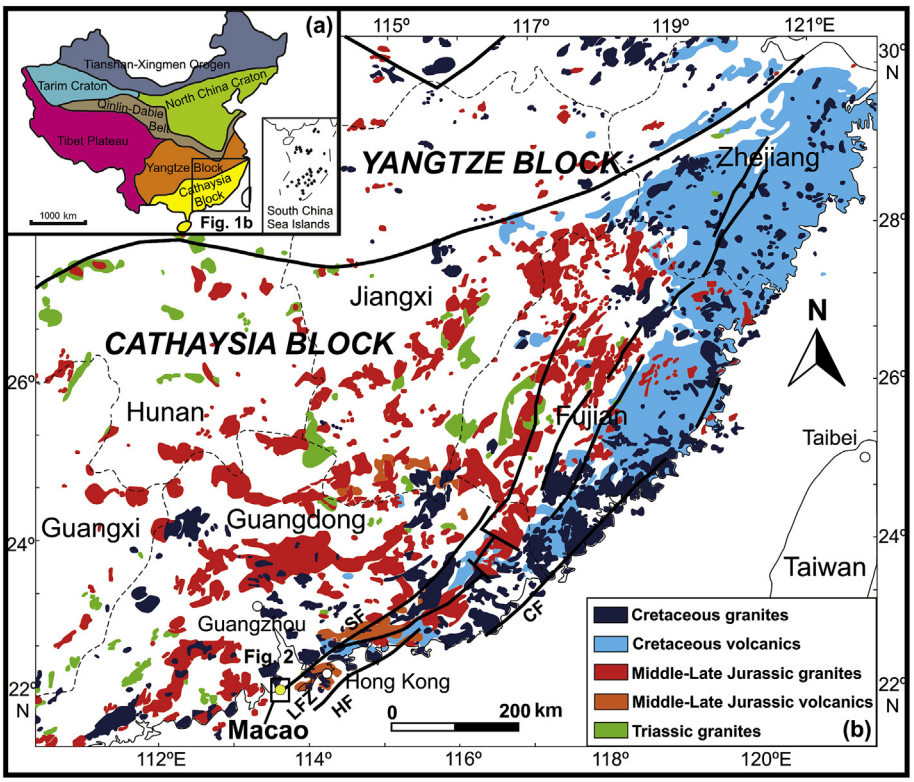

Fig. 1. (a) Simplified tectonic sketch of China; (b) geological map of SE China, showing the distribution of Mesozoic granitic and volcanic rocks on the Cathaysia Block. The Lianhuashan Fault Zone (LFZ), Shenzhen Fault (SF), Haifeng Fault (HF) and Changle–Na'nao Fault (CF) are also represented. Figure adapted from Davis et al. (1997) and Zhou et al. (2006).

magmatic evolution during the Yanshanian orogeny. In contrast, more detailed work was done in the neighboring region of Hong Kong, where high-precision U–Pb zircon geochronology constrained the Jurassic–Early Cretaceous magmatism (165–141 Ma) to four main pulses correlated with important tectonic events within the Yanshanian orogeny (Sewell et al., 1992, 2012).

Despite its relatively small area (~30 km^2), the Macao territory includes a wide range of granitic facies with different textures, mineralogy and compositions. The first dating of Macao granitic rocks was obtained on biotite using the Potassium (K)–Argon (Ar) method, with most samples dated between 154 ± 5 Ma and 168 ± 4 Ma. A significantly younger date of 94 ± 2 Ma was also reported (Ribeiro et al., 1992, 2010). However, the number of samples analyzed was not enough to encompass the variety of granitic facies outcropping in the territory and did not include the hypabyssal dykes intruding the granites. Besides, the K–Ar method has some inherent limitations resulting from post-magmatic Ar loss or gain, which may lead to erroneous ages (e.g., Cobbing, 2000; Gillot et al., 2006; Lee, 2014). U–Pb zircon dating is now the first choice for dating granites, providing the basis for accurate and precise age determination given: (1) the lack of significant Pb incorporation during crystallization (Harley and Kelly, 2007; Scherer et al., 2007); (2) its high blocking temperature (>900 °C; e.g., Scherer et al., 2007); and (3) extremely low Th, U and Pb diffusion rates (e.g., Cherniak et al., 1997; Lee et al., 1997). For these reasons, zircon has been considered the best deep-time archive of Earth's continental crust (Davis et al., 2003; Roberts and Spencer, 2015).

In this study, a large number of zircon grains from the Macao granites were dated. Two methods were employed: isotope dilution thermal ionization mass spectrometry (ID-TIMS) and laser ablation multi-collector inductively coupled plasma mass spectrometry (LA-MC-ICPMS). While ID-TIMS is the most precise and most accurately calibrated method for the determination of crystallization ages of zircon, LA-MC-ICPMS is a fast, yet reasonably accurate and precise, technique, making it easy to obtain large numbers of analyses with a good spatial resolution (10–60 μm spot size, 5–20 μm depth) that allows better assessment of inheritance. Both methods combined provided a robust age data set for the Macao magmatic rocks. The new data set includes not only different granitic facies from each of the three main outcropping areas in Macao (Macao Peninsula, Taipa and Coloane), but also the post-granite dacite dykes. We use these data to verify the validity of the previous ages attributed to Macao granitic rocks, to know the age of a larger number of granitic facies and other magmatic rocks, to investigate the periodicity of magmatism in the territory and to contribute to a better knowledge of the tectono-thermal evolution of the Yanshanian orogeny.

2. Geological background

The South China Block (SCB) was formed during the Early Neoproterozoic, by amalgamation of the Cathaysia Block in the southeast and the Yangtze Block in the northwest along the Jiangshan-Shaoxing suture zone (Fig. 1; e.g., Li et al., 2002; Ye et al., 2007; Charvet, 2013; Wang et al., 2013). While the Yangtze Block has an Archean to Paleoproterozoic basement (e.g., Qiu et al., 2000; Zheng et al., 2006), the oldest basement of Cathaysia Block is represented by sporadic Paleoproterozoic rocks outcropping in the eastern part (e.g., Li, 1997; Li et al., 2000; Yu et al., 2012; Liu et al., 2014). In the western part, the outcropping Precambrian basement consists of Neoproterozoic igneous rocks and sedimentary strata (e.g., Zhang and Zheng, 2013; Li et al., 2014). The Cathaysia Block has been episodically reworked by the Jiangnan (Neoproterozoic),

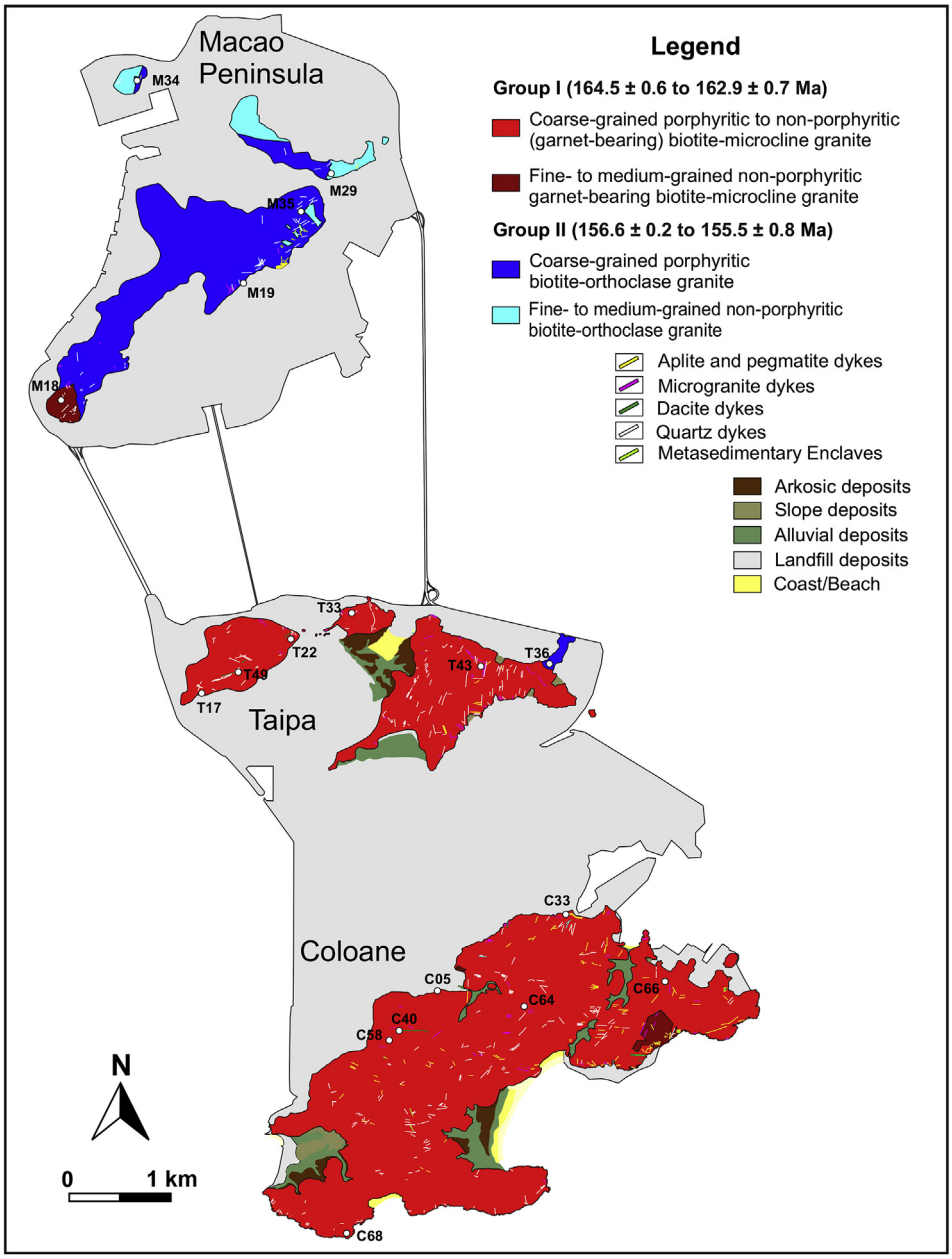

Fig. 2. Simplified geological map of Macao showing the distribution of the two groups of granites in the territory and the location of samples chosen for geochronology. Two main groups of granites are distinguished based on the determined ages and petrographic characteristics. See main text for details.

Wuyi–Yunkai (Early Paleozoic), Indosinian (Triassic) and Yanshanian (Late Mesozoic) tectono-thermal events (e.g., Li, 1998; Wang et al., 2013).

Macao is located on the SE China coast, south of Guangdong Province, about 50 km west of Hong Kong. In this area, there is a predominance of granitic intrusions that belong to a ~3500 km long and ~800 km wide NE-trending magmatic belt cropping out on the SE part of the Cathaysia Block (Fig. 1). Its origin has been associated with the Yanshanian orogeny, related to the Late Mesozoic subduction of the Paleo-Pacific plate under the Eurasian plate (e.g., Lapierre et al., 1997; Zhou and Li, 2000; Zhou et al., 2006; Li and Li, 2007; Jiang et al., 2009, 2015). In the neighboring region of Hong Kong, the Jurassic–Early Cretaceous magmatism occurred in four main pulses constrained by high-precision zircon U–Pb geochronology: 165–160 Ma (Lamma Suite), 148–146 Ma (Kwai Chung Suite), 143 Ma (Cheung Chau Suite) and 141 Ma (Lion Rock Suite) (Sewell et al., 1992, 2012). These magmatic pulses record a temporal evolution of magma compositions indicative of a transition from a compression-related to an extension-related tectonic regime (Sewell et al., 1992), consistent with the tectono-magmatic evolution of SE China (Zhou et al., 2006). Yanshanian magmatism probably continued in Hong Kong area until ca. 100–80 Ma, ceasing with the beginning of continental arc collapse, a consequence of the large-scale crustal extension in the region (Tang et al., 2014).

One of the most important tectonic structures in the coastal region of SE China is the NE-trending Lianhuashan Fault Zone, which can be traced for over 400 km through the coastal provinces of SE China (Chen, 1987; Ding and Lai, 1997). Near Macao and Hong Kong, the Lianhuashan Fault Zone comprises a 30 km wide zone limited to the North by the Shenzhen Fault and to the south by the

Haifeng fault (Chen, 1987; Huang and Zhang, 1990; Fig. 1b). Several volcanic centers and plutonic assemblages occur associated with the Lianhuashan Fault Zone, suggesting that it was a major locus of magmatic activity during the Late Mesozoic (Campbell and Sewell, 1997; Davis et al., 1997; Sewell and Campbell, 1997; Xia and Zhao, 2014).

In Macao, the plutonic rocks mainly consist of biotite granites with variable petrographic, mineralogical and geochemical features (Fig. 2). They intrude into the Paleozoic strata, of dominant Devonian age (Ribeiro et al., 1992). Some remnants of the wall rocks are found in the territory as sparse metasedimentary enclaves within the granites. In addition, Microgranular Mafic Enclaves (MMEs) of variable size and shape are common within the granites.

The granites are cut by a swarm of granitic dykes (microgranite, aplite and pegmatite) and dacite dykes. The former usually show irregular contours and diffuse contacts with the host granite, while the latter show sharp contacts.

3. Analytical methods

3.1. Mineral and whole-rock elemental chemistry

Mineral analyses were performed on carbon-coated polished thin sections using a JEOL SUPERPROBE™, model JXA-8200, in wavelength dispersive mode at the Departamento de Geologia da Faculdade de Ciências da Universidade de Lisboa (Portugal). Minerals were analyzed with an acceleration voltage of 15 kV and a current of 25 nA, using a 5 μm wide beam. The analyses performed in each mineral phase were calibrated using the composition of reference materials, with reproducibility errors being lower than 2% and ordinarily around 1%. Matrix effects were corrected using the ZAF software provided by JEOL. Information about standards and detection limits are given in Supplementary File 1A.

Whole-rock major and trace element concentrations were obtained at Activation Laboratories, Ltd. (Ancaster, Ontario, Canada) using the geochemical analytical package 4E - Research - INAA, Total Digestion - ICP, Lithium Metaborate/Tetraborate Fusion - ICP, plus ICP-MS for some of the trace elements. Major oxide content was analyzed by Inductively Coupled Plasma-Optical Emission Spectrometry (ICP-OES) using a Thermo Jarrell-Ash ENVIRO II ICP and/or Spectro Cirros ICP. Trace elements, including Rare Earth Elements (REE), were obtained using Inductively Coupled Plasma Mass-Spectrometry (ICP-MS) on a PerkinElmer SCIEX ELAN 6000, 6100 or 9000 ICP/MS and by Instrumental Neutron Activation Analysis (INAA). In-house standards and several certified reference materials of granitic to dioritic compositions (s.l.) from USGS (United States Geological Survey), GSJ (Geological Survey of Japan) and CCRMP (Canadian Certificate Reference Material Project) were used. Errors associated with the accuracy are ≤4% for major elements and better than 9% for the REE and the most widely used incompatible elements. Duplicate measurements of samples indicate that errors associated with reproducibility were generally lower than 5% for both major and trace elements. Information about detection limits is given in Supplementary File 1B. For detailed information regarding analytical and control procedures consult the Actlabs website (www.actlabs.com).

3.2. Geochronology

3.2.1. Zircon separation

Representative samples from the different magmatic facies identified through fieldwork and petrographic analysis were selected for zircon separation procedures. Samples were repeatedly crushed with a jaw crusher to obtain ca. 100 μm sized grains. Zircon grains were isolated using standard heavy liquids and magnetic techniques. Initial separation involved multiple passes of crushed rock over a Wilfley table to concentrate heavy minerals. Further zircon concentration was achieved by using heavy liquids (bromoform and methylene iodide) enabling density separation and a Frantz isodynamic magnetic separator. Final grains selection was made by hand picking under a binocular microscope, choosing the freshest, least-cracked zircon grains (see sections 3.2.2. and 3.2.3).

3.2.2. ID-TIMS

The isotope dilution (ID) - thermal ionization mass spectrometry (TIMS) analyses were performed at Jack Satterly Geochronology Laboratory, Department of Geology, University of Toronto, Toronto, Ont., Canada.

Zircon crystals were mounted in epoxy and polished to check for the possibility of xenocrystic cores. Grains were imaged with backscattered electrons (BSE) and cathodoluminescence (CL) using a JEOL JSM6610-Lv scanning electron microscope. Crystal domains that are high in U, and therefore relatively damaged by radiation, are bright under BSE and dark under CL, with the opposite for low U domains (Hanchat and Miller, 1993). Alteration shows as dark amorphous domains and is usually only seen in highly damaged zircon.

The freshest and least-cracked whole grains were hand-picked for analysis using an optical microscope. Chemical abrasion (CA, Mattinson, 2005) was used to remove any discordant domains. For CA treatment, zircon grains were annealed in quartz crucibles at 1000 °C overnight. These crystals were then leached for 6 h in concentrated hydrofluoric acid (HF) at 200 °C in Teflon bombs, the same conditions under which they are dissolved but for a shorter period, followed by leaching in 3N HCl overnight in Teflon bombs to dissolve any REE-rich fluoride phases that might inhibit equilibration with the spike. The annealing partially heals radiation damage in the zircon, rendering it more chemically inert and slowing its rate of dissolution in HF. Altered crystal domains, which contain disturbed Pb and are responsible for discordance, dissolve faster than annealed unaltered zircon and are usually completely removed after a few hours of leaching. Relatively undamaged crystals such as these are attacked only slightly by the leaching process, in some cases showing surface etching and white coloration along cracks. Fragments were chosen to contain as little white discoloration as possible. In cases where there is noticeable etching, the presence of a small amount of discoloration does not seem to affect the results.

To minimize the possibility of inheritance, single zircon grains were analyzed having characteristics typical of the igneous population, such as a euhedral shape and an abundance of melt or rod-like inclusions. Weights of zircon grains selected for ID-TIMS analyses were estimated from photomicrographs. Estimated weights should be accurate to about ±30%. This affects only U and Pb concentrations, not age information, which depends only on isotope ratio measurements. Washed zircon was dissolved using concentrated HF in Teflon bombs at 200 °C for 5 days (Krogh, 1973). Samples were subsequently redissolved in 3N HCl along with ^{205}Pb—^{233}U—^{235}U (ET535) spike. U and Pb were separated from the solutions using 50 μL anion exchange columns (Krogh, 1973). Mixed purified U and Pb solutions were loaded directly onto Re filaments using silica gel and analyzed with a VG354 mass spectrometer in multi-collector static Faraday and single collector Daly mode. Dead time of the Daly measuring system is 16.5 ns. The mass discrimination correction for the Daly detector is constant at 0.06% per AMU. For samples that were large enough, U and Pb were analyzed in static mode using multiple Faraday cups with mass 204 in the axial Daly. Smaller samples were analyzed in peak jumping mode on the Daly collector. Faraday amplifiers were calibrated daily. Daly gains were calibrated at the beginning of each sample. $^{207}Pb/^{205}Pb$

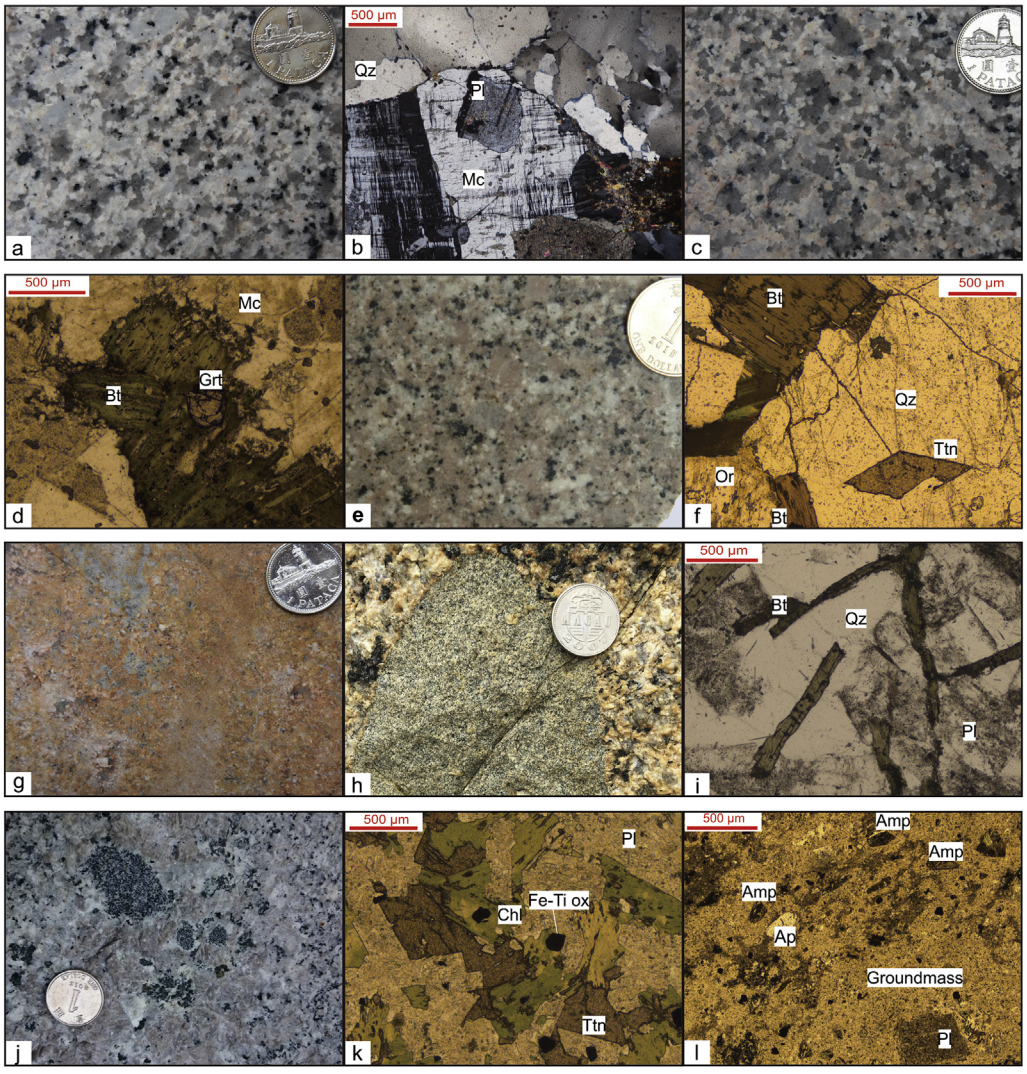

Fig. 3. Hand specimens and thin sections representative of the different lithofacies observed in Macao: (a) Group I coarse-grained porphyritic biotite-microcline granite; (b) poikilitic perthitic microcline megacrysts enclosing smaller plagioclase crystals in Group I; (c) Group I coarse-grained non-porphyritic garnet-bearing biotite-microcline granite; (d) accessory garnet growing at expense of biotite, common in highly fractionated granites from Group I; (e) Group II coarse-grained porphyritic biotite-orthoclase granite; (f) a well-developed euhedral titanite crystal common in Group II weakly fractionated granites; (g) Group II fine-grained biotite-orthoclase granite; (h) MME enclosed in Group I granites; (i) Group I MME with acicular biotite; (j) MME enclosed in Group II granites; (k) Group II MME with lozenge-shaped strongly chloritized biotite and titanite; (l) dacite dyke with amphibole and plagioclase phenocrysts within a feldspathic groundmass. MME: mafic microgranular enclave; Amp: amphibole; Ap: apatite; Fe–Ti ox: Fe–Ti oxides; Qz: quartz; Pl: plagioclase; Or: orthoclase; Ttn: titanite; Bt: biotite; Chl: chlorite; Mc: microcline; Grt: garnet.

ratios were measured in peak jumping mode on the Daly near the end of Pb emission to improve precision over static values, where the ^{207}Pb peak is too small for precise measurement using the Faraday collector. Isobaric interferences are monitored at mass 210 and typically show a gradual decrease throughout a run. They are only significant for the small 204 mass peak. Consequently, the $^{207}Pb/^{204}Pb$ ratio generally shows an increase with time. The $^{207}Pb/^{204}Pb$ ratio is measured by peak jumping on the Daly collector at the end of the Pb run when the mass 210 is at baseline. U isotopes are measured at higher temperature in static mode with the Faraday collectors. The $^{233}U/^{235}U$ ratio from the spike allows correction for analytical mass fractionation. Pb isotopes cannot be corrected for analytic mass fractionation, but silica loads are known to have a predictable Pb mass fractionation that begins at about 0.13% per AMU and decreases to about 0 as the load is exhausted. The fractionation correction is taken to be 0.1% ± 0.04% per AMU. This sets a limit on age precision for precisely analyzed samples.

3.2.3. LA-MC-ICPMS

The laser ablation (LA) multi-collector (MC) inductively coupled plasma source mass spectrometer (ICPMS) analyses were performed at the Department of Earth Sciences of the University of Hong Kong.

Individual zircon grains were hand-picked under a binocular microscope, then mounted in standard 1" epoxy mounts and polished. To characterize the internal structures of the zircons, BSE images were obtained using a JEOLJXA-8100 microprobe at the Department of Earth Sciences of the University of Hong Kong.

Zircon grains were analyzed with a Nu Plasma HR MC-ICPMS (Nu Instruments, UK), coupled with a 193 nm excimer laser ablation system (RESOlution M-50, Resonetics LLC, USA). It combines rapid (<1.5 s for 99%) signal washout with full flexibility in sample size (50 mm × 50 mm × 25 mm) and high sensitivity (>10000 cps/ppm for mid-high m/z, 55 mm, 5 Hz). The MC-ICPMS contains twelve F collectors and four ion counting detectors dispersed on the

Table 1
Representative chemical compositions of biotites from Macao granites.

Sample	c51b_fb_bt6	c58_b2_bt2	c60_b1_bt6	c71_b4_bt5	m16_b2_bt1	t17_b4_bt2	m29b_b5_bt1	m6_b5_bt2	m11_b5_bt2	m6_b3_bt1	m29b_b5_bt2	m20_b1_bt3
Group	GI	GI	GI	GI	GI	GI	GII	GII	GII	GII	GII	GII
Fractionation degree	WMF	WMF	WMF	HF	HF	HF	WMF	WMF	WMF	WMF	WMF	HF
Oxides (wt.%)												
SiO_2	36.94	36.72	36.37	35.54	36.83	37.16	36.71	36.19	37.12	37.33	35.35	37.36
TiO_2	2.03	1.77	1.64	2.08	2.69	2.43	3.17	3.25	2.70	3.16	2.70	3.11
Al_2O_3	15.45	16.05	16.22	17.19	14.00	17.39	14.54	13.67	14.04	13.48	15.41	14.04
FeO	22.38	24.19	24.15	28.00	23.03	21.73	21.84	24.18	20.31	22.72	22.83	22.27
Fe_2O_3	2.66	2.70	2.72	2.98	2.78	0.95	3.08	3.52	3.29	3.90	4.16	2.38
MnO	0.63	0.86	0.93	0.54	1.79	1.28	0.66	1.05	0.57	0.72	0.84	1.32
MgO	6.43	4.41	4.88	1.20	5.39	3.32	6.85	6.05	9.66	6.18	7.08	6.90
CaO	0.05	0.03	0.03	0.01	0.02	0.00	0.06	0.05	0.36	0.61	0.04	0.01
Na_2O	0.07	0.05	0.03	0.09	0.21	0.08	0.25	0.09	0.07	0.08	0.11	0.10
K_2O	10.13	10.11	10.11	9.93	9.93	10.22	9.13	9.02	9.00	8.16	7.18	10.00
BaO	0.01	0.05	0.09	0.01	0.07	0.00	0.34	0.38	0.06	0.04	0.30	0.50
F*	1.26	0.58	0.87	0.02	2.13	1.93	0.71	0.49	0.69	0.57	0.71	0.69
Cl*	0.05	0.04	0.03	0.09	0.20	0.12	0.12	0.15	0.07	0.13	0.08	0.09
Cr_2O_3	0.10	0.07	0.07	0.09	0.04	0.07	0.09	0.07	0.09	0.10	0.05	0.09
Total	97.65	97.36	97.75	97.73	98.16	95.84	97.24	97.90	97.71	96.89	96.52	98.57
Cations per 22 oxygens												
Si	5.77	5.78	5.72	5.67	5.83	5.84	5.75	5.73	5.73	5.88	5.60	5.79
Al^{iv}	2.23	2.22	2.28	2.33	2.17	2.16	2.25	2.27	2.27	2.12	2.40	2.21
Al^{vi}	0.62	0.76	0.73	0.90	0.44	1.06	0.43	0.28	0.28	0.39	0.48	0.35
Ti	0.24	0.21	0.19	0.25	0.32	0.29	0.37	0.39	0.31	0.37	0.32	0.36
Cr	0.01	0.01	0.01	0.01	0.00	0.01	0.01	0.01	0.01	0.01	0.01	0.01
Fe^{2+}	2.92	3.19	3.18	3.74	3.05	2.86	2.86	3.20	2.62	3.00	3.03	2.89
Fe^{3+}	0.16	0.16	0.16	0.18	0.17	0.06	0.18	0.21	0.19	0.23	0.25	0.14
Mn	0.08	0.11	0.12	0.07	0.24	0.17	0.09	0.14	0.07	0.10	0.11	0.17
Mg	1.50	1.03	1.14	0.28	1.27	0.78	1.60	1.43	2.22	1.45	1.67	1.59
Ca	0.01	0.00	0.00	0.00	0.00	0.00	0.01	0.01	0.06	0.10	0.01	0.00
Na	0.02	0.02	0.01	0.03	0.07	0.02	0.08	0.03	0.02	0.02	0.03	0.03
K	2.02	2.03	2.03	2.02	2.01	2.05	1.82	1.82	1.77	1.64	1.45	1.98
Ba	0.00	0.00	0.01	0.00	0.00	0.00	0.02	0.02	0.00	0.00	0.02	0.03
F	0.62	0.29	0.43	0.01	1.07	0.96	0.35	0.24	0.34	0.29	0.35	0.34
Cl	0.01	0.01	0.01	0.02	0.05	0.03	0.03	0.04	0.02	0.03	0.02	0.02
Total	16.22	15.83	16.03	15.52	16.70	16.28	15.86	15.81	15.93	15.64	15.75	15.93

Abbreviations: GI—Group I granites; GII—Group II granites; WMF—Weakly to moderately fractionated (Zr/Hf > 25); HF—highly fractionated (Zr/Hf < 25).
The values of Fe^{2+} and Fe^{3+} are estimated by the approach of Bruiyn et al. (1983).

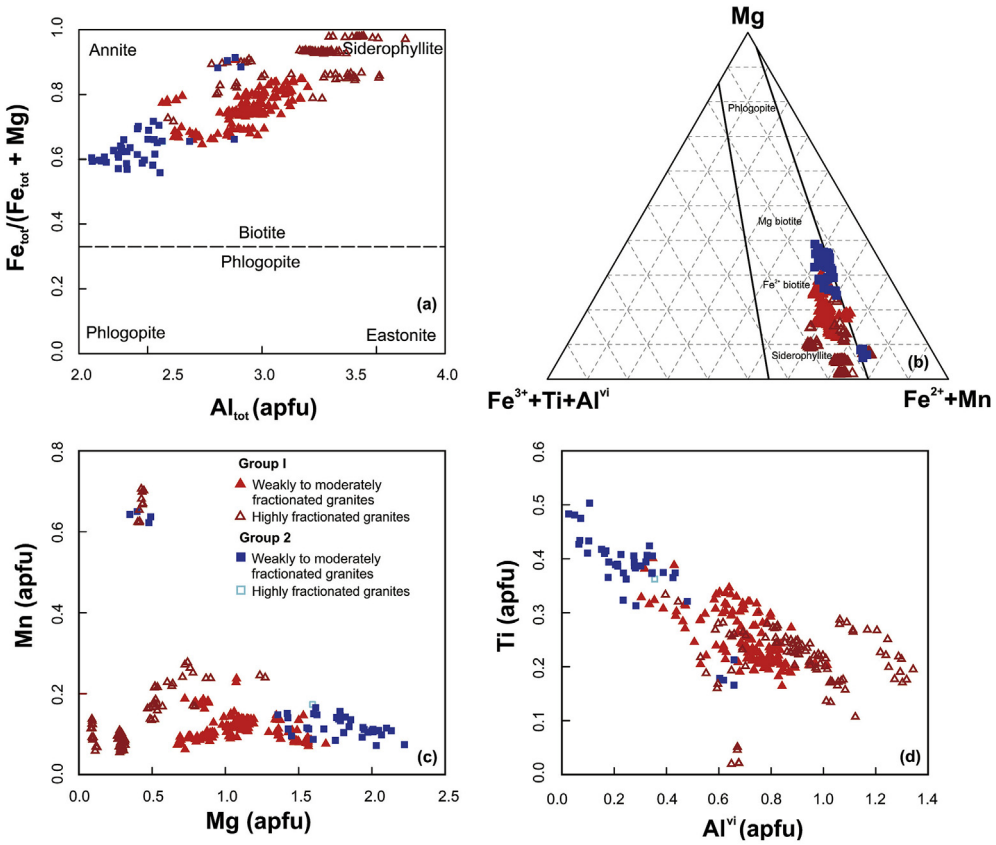

Fig. 4. Chemistry of biotites from the Macao granites: (a) $Fe_{tot}/(Fe_{tot} + Mg)$ vs. Al_{tot} diagram, also known as the annite (Ann) – siderophyllite (Sdp) – phlogopite (Phl) – eastonite (Eas) quadrilateral diagram; Fe_{tot}: total iron, i.e., $Fe^{2+} + Fe^{3+}$; (b) octahedral cations in the classification diagram of Foster (1960); (c) Mn vs. Mg variation diagram; (d) Ti vs. Al^{vi} variation diagram.

low mass side of the array, allowing simultaneous acquisition of ion signals ranging from mass ^{238}U, ^{232}Th, ^{208}Pb, ^{207}Pb, ^{206}Pb and ^{204}Pb. Instrument parameters and analytical details are described in Xia et al. (2011). In this study, beam diameter of 30 μm, repetition rate of 4 Hz and energy density of 5 J/cm^2 on sample surface were used. The machine measured the background signal around 15 s and ablation time 25 s, resulting in pits ~20 μm deep. The standard zircons 91500 (Wiedenbeck et al., 1995) and GJ-1 (Jackson et al., 2004) were measured every 10–15 unknown measurements for further calibration. The instrument configuration does not measure other elements, so no concentrations are given.

In most cases, the border of the crystals was analyzed to ensure that a crystallization age was obtained, since the outermost part of zircon crystals usually corresponds to the more recent magmatic events. To avoid possible inheritance, the most internally homogenous grains were chosen for crystallization age determination. However, it must be considered that zircon grains often represent a continuum of crystallization ages and due to diameter of the laser (30 μm) some mixing cannot be totally avoided.

4. Analytical results

4.1. Petrography

Overall, Macao biotite granites are mainly composed of quartz (30–35 vol%), K-feldspar (35–40 vol%), plagioclase (20–25 vol%) and biotite (5–10 vol%). According to the type of K-feldspar, they can be divided into microcline granites (Group I; Fig. 3a–d) and orthoclase granites (Group II; Fig. 3e–g), which are also distinct in age (section 5.1; see also Fig. 2). In both groups, textures vary from medium- to coarse-grained porphyritic to fine-grained non-porphyritic moderately equigranular.

K-feldspar occurs as euhedral to subhedral megacrysts (Fig. 3a, b and e) or heterogranular subhedral to anhedral crystals in the groundmass. It ranges up to 7 cm long and consists of perthite that commonly contains small inclusions of plagioclase and quartz. The K-rich phase portrays distinct structures, microcline in Group I granites and orthoclase in Group II, recognizable by the typical tartan pattern (albite/pericline twins; Fig. 3b) and Carlsbad twining, respectively. Plagioclase occurs as subhedral tabular crystals (<1 cm) with polysynthetic albite twinning, showing normal and oscillatory zoning under the microscope. Biotite is anhedral to subhedral, occurring as interstitial isolated slab-flake crystals or in mineral clusters, often containing a wide variety of accessory minerals. Its modal percentage tends to decrease from the porphyritic facies towards the fine-grained equigranular facies. Quartz is anhedral and heterogranular (<0.7 cm), in some cases forming graphic and myrmekitic intergrowths with K-feldspar and plagioclase, respectively. At odds with Group II granites, quartz grains from Group I show evidence for significant deformation such as pervasive undulatory extinction, sutured grain boundaries and development of individual subgrains with well-defined boundaries (Fig. 3b).

While many accessory minerals are common in both groups (Fe–Ti oxides, apatite, zircon, monazite, xenotime, allanite, sulfides and fluorite), titanite (Fig. 3f) is distinctly more abundant in Group II granites whereas garnet and abundant tantalo-niobates are characteristic of Group I granites. Zircon usually occurs as

Table 2
Representative whole-rock major and trace element compositions of the Macao granites and dacites.

Sample	C 66	T 33	M18	T44	M 19	M 25	M 31	M 30	C40
Group	GI	GI	GI	GI	GII	GII	GII	GII	Dacite
Fractionation degree	WMF	WMF	HF	HF	WMF	WMF	HF	HF	WMF
Major elements (wt.%)									
SiO_2	73.45	72.46	75.44	75.72	68.19	74.89	76.51	75.23	63.61
Al_2O_3	13.73	13.43	12.42	12.68	14.80	12.96	12.82	12.98	16.61
$Fe_2O_3^t$	2.34	2.70	1.42	1.34	3.30	1.65	1.35	1.46	4.17
MnO	0.06	0.09	0.05	0.04	0.08	0.03	0.03	0.02	0.10
MgO	0.22	0.34	0.08	0.02	0.53	0.14	0.08	0.07	1.62
CaO	1.26	1.19	0.76	0.50	1.97	0.88	0.63	0.53	4.01
Na_2O	3.17	3.25	3.70	3.96	2.89	3.18	3.40	3.42	3.62
K_2O	5.06	4.82	4.54	5.00	5.36	4.74	4.91	4.68	2.56
TiO_2	0.16	0.20	0.06	0.02	0.39	0.14	0.08	0.09	0.47
P_2O_5	0.04	0.08	0.01	0.00	0.13	0.04	0.02	0.00	0.28
LOI	0.79	0.80	0.32	0.09	1.43	0.90	0.67	0.75	2.70
Total	100.30	99.36	98.80	99.37	99.07	99.53	100.50	99.24	99.73
Trace elements (ppm)									
Ba	230.00	393.00	91.00	15.00	625.00	103.00	23.00	35.00	1179.00
Be	6.00	6.00	7.00	13.00	9.00	6.00	7.00	8.00	2.00
Bi	0.30	0.80	0.10	0.30	0.50	0.80	0.30	0.00	0.10
Co	4.00	7.00	1.70	0.00	7.40	4.00	0.80	2.70	6.80
Cr	121.00	165.00	103.00	50.00	71.70	82.10	75.10	108.00	81.00
Cs	14.70	12.00	8.70	10.60	9.60	7.50	7.80	6.10	10.70
Cu	10.00	16.00	6.00	5.00	56.00	17.00	22.00	12.00	2.00
Ga	17.00	19.00	18.00	21.00	18.00	16.00	16.00	16.00	19.00
Ge	2.00	1.70	2.10	3.30	1.70	2.00	2.00	1.90	1.50
Hf	4.30	5.00	3.80	5.60	5.30	3.60	3.50	1.90	3.90
Nb	16.40	16.00	20.20	27.80	13.50	11.50	14.60	11.00	6.80
Ni	57.00	77.00	39.00	29.00	28.00	41.00	37.00	35.00	42.00
Pb	42.00	42.00	44.00	53.00	31.00	39.00	51.00	42.00	9.00
Rb	356.00	373.00	384.00	416.00	371.00	414.00	455.00	388.00	143.00
Sb	0.40	0.50	0.00	0.30	0.10	0.30	0.30	0.20	0.30
Sc	4.80	5.10	3.78	2.27	6.60	2.80	2.90	2.00	7.19
Sn	11.00	70.00	7.00	6.00	628.00	141.00	86.00	5.00	1.00
Sr	84.00	121.00	38.00	9.00	210.00	57.00	25.00	36.00	1104.00
Ta	3.25	3.00	7.26	9.82	2.31	2.43	2.40	2.12	0.51
Th	36.80	37.60	24.80	19.60	30.10	33.20	33.70	27.40	5.01
U	21.30	11.30	16.80	31.00	12.10	16.00	18.90	21.00	0.99
V	12.00	16.00	5.00	5.00	32.00	11.00	0.00	6.00	59.00
W	0.00	14.00	3.00	0.00	51.00	6.00	1.00	0.00	0.00
Y	58.00	38.00	88.00	94.00	32.00	39.00	24.00	31.00	16.00
Zn	39.00	41.00	24.00	9.00	44.00	25.00	18.00	10.00	45.00
Zr	127.00	170.00	77.00	70.00	191.00	97.00	79.00	31.00	157.00
La	32.40	49.50	14.20	8.34	43.10	30.50	13.50	24.00	35.70
Ce	69.50	100.00	32.40	21.60	91.20	44.10	28.30	25.30	68.80
Pr	7.98	10.80	4.29	3.34	10.20	6.82	3.03	5.08	7.95
Nd	28.90	37.30	17.60	14.50	36.10	23.30	9.81	16.50	29.70
Sm	7.87	7.61	7.28	7.64	7.27	5.27	2.26	3.84	5.15
Eu	0.65	0.75	0.29	0.09	1.20	0.58	0.18	0.40	1.56
Gd	7.89	7.41	9.62	8.93	6.29	5.15	2.60	3.77	3.91
Tb	1.42	1.17	2.00	2.01	0.95	0.88	0.48	0.66	0.52
Dy	9.47	7.14	13.70	13.90	5.79	5.78	3.13	4.39	2.97
Ho	1.94	1.39	2.79	2.97	1.17	1.22	0.74	0.98	0.57
Er	6.04	4.06	8.79	10.00	3.64	4.04	2.78	3.20	1.74
Tm	0.93	0.62	1.50	1.86	0.59	0.68	0.50	0.58	0.27
Yb	6.43	4.31	10.40	14.20	4.29	5.37	4.48	5.01	1.75
Lu	0.96	0.67	1.64	2.28	0.71	0.91	0.86	0.87	0.28
Tl	1.71	1.68	1.85	1.77	1.85	1.84	1.79	1.68	1.09
Eu/Eu*[a]	0.25	0.30	0.11	0.03	0.54	0.34	0.23	0.32	1.06
Ti/Ti*[b]	0.04	0.05	0.02	0.01	0.08	0.04	0.06	0.04	0.12
$TE_{1,3}$[c]	1.04	1.03	1.07	1.13	1.03	0.97	0.90	1.07	-

Abbreviations: GI–Group I granites; GII–Group II granites; WMF–weakly to moderately fractionated (Zr/Hf > 25); HF–highly fractionated (Zr/Hf < 25).

[a] The Eu anomaly is the ratio between measured Eu and the value expected for Eu on a smooth chondrite-normalized plot (Eu*), where $Eu^* = \sqrt{(Sm_N \times Gd_N)}$. If this ratio is > 1 the anomaly is positive, if the ratio is < 1 the anomaly is negative.

[b] The Ti anomaly is the ratio between measured Ti and the value expected for Ti on a smooth chondrite-normalized plot (Ti*), where $Ti^* = \sqrt{(Eu_N \times Dy_N)}$. If this ratio is > 1 the anomaly is positive, if the ratio is < 1 the anomaly is negative.

[c] The term 'tetrad effect' refers to the subdivision of the fifteen lanthanide elements into four groups called tetrads: (1) La–Nd, (2) Pm–Gd, (3) Gd–Ho, and (4) Er–Lu, each tetrad forming a smooth convex (M-type) or concave (W-type) pattern. Degree of the tetrad effect = $TE_{1,3} = (t1 \times t3)_{0.5}$, where $t1 = (Ce/Ce^t \times Pr/Pr^t)^{0.5}$ and $t3 = (Tb/Tb^t \times Dy/Dy^t)^{0.5}$, with $Pr/Pr^t = Pr_N/(La_N^{1/3} \times Nd_N^{2/3})$, $Tb/Tb^t = Tb_N/(Gd_N^{2/3} \times Ho_N^{1/3})$ and $Dy/Dy^t = Dy_N/(Gd_N^{1/3} \times Ho_N^{2/3})$.

inclusions in biotite surrounded by pleochroic haloes and, more rarely, as isolated grains in the groundmass interstitial to K-feldspar and plagioclase.

The MMEs (Fig. 3h–k) are mainly hosted by the porphyritic coarse-grained granitic facies, varying from monzogranite to granodiorite in Group I granites to quartz monzodiorite in Group II. They range from a few millimeters up to <1 m in size. In the field, they commonly have sharp contacts with their host, are irregular to oval blobs and locally occur as dike-like trails. Textures vary from slightly porphyritic to equigranular fine-grained. Compared with the host granite, MMEs generally contain the same mineral assemblage but with higher contents of biotite (in some cases highly chloritized; Fig. 3k) and plagioclase, and lower contents of quartz and K-feldspar.

The dacite dykes are slightly porphyritic with euhedral to subhedral tabular plagioclase (<0.5 cm) and prismatic hornblende (<0.1 cm) phenocrysts within an aphanitic matrix composed of K-feldspar and microcrystalline quartz and minor Fe–Ti oxides, zircon and apatite (Fig. 3l). Alteration of feldspars produces pervasive sericite.

4.2. Mineral and whole-rock elemental chemistry

Representative electron microprobe analyses of biotites from the studied samples are displayed in Table 1. According to the nomenclature of micas (Speer, 1984; Deer et al., 1992; Rieder, 1999), biotites from Macao granitic rocks show a wide range of compositions between Mg-rich annite and Fe-rich siderophyllite (Fig. 4a and b).

Representative whole-rock major and trace element analyses of the Macao granites are shown in Table 2. They have variable SiO_2 contents (66.77–76.92 wt.%), moderate total alkali ($K_2O + Na_2O$ = 7.04–8.54 wt.%) and K_2O/Na_2O = 1.24–1.62, being classified as high-K calc-alkaline rocks. According to their molar $Al_2O_3/(CaO + Na_2O + K_2O)$ ratios, these rocks are metaluminous to weakly peraluminous (A/CNK = 0.96–1.13). REE compositions are highly variable with $(La/Yb)_N$ ratios ranging from 0.12 to 10.76 (Fig. 5) and negative Eu anomalies (Eu/Eu^*) from 0.02 to 0.54 (Table 2). They are also characterized by a wide range of Zr/Hf ratios (12.24–37.60). Since Zr/Hf ratios tend to decrease with increasing evolution of high-silica melts (e.g., Irber, 1999), some authors have suggested this ratio as a granite fractionation index (e.g., Bea et al., 2006; Zaraisky et al., 2009). Therefore, in this study, we consider weakly to moderately fractionated granites those having Zr/Hf > 25, while highly fractionated granites are marked by comparatively lower Zr/Hf ratios (≤25).

The dacite dykes have lower SiO_2 contents (63.61–65.27 wt.%) and total alkali contents ($K_2O + Na_2O$ = 5.05–6.18 wt.%) than the granites. They are enriched in large ion lithophile elements (LILE) relatively to high field strength elements (HSFE) with high Rb/La ratios of 4.3–8.5, have high $(La/Yb)_N$ ratios of 11.45–13.86 and positive Eu anomalies (Eu/Eu^* = 1.06–1.13; Table 2).

4.3. ID-TIMS geochronology

Six samples were analyzed for U–Pb zircon geochronology using ID-TIMS (Tables 3 and 4, Figs. 6 and 7; see also Supplementary File 2 for details on the location and general characteristics of the analyzed samples). Detailed descriptions of zircons from each sample and BSE and CL images are provided in Supplementary File 3. Mass spectrometer data were reduced using in-house software (UTILAge program written by D.W. Davis). Concordia data are plotted using the Isoplot program of Ludwig (1998, 2012). Individual analyses in the data table (Table 3) and concordia plots are presented as 2σ absolute error and uncertainties in averages ages are quoted at the 95% level (2σ). Ages are based on $^{206}Pb/^{238}U$ ratios, which are least susceptible to analytical bias and should give robust age estimates within the quoted errors. Data may in some cases scatter slightly to the left of the concordia curve due to residual interferences affecting the small ^{204}Pb peak, which causes an overcorrection for common Pb but does not significantly affect the

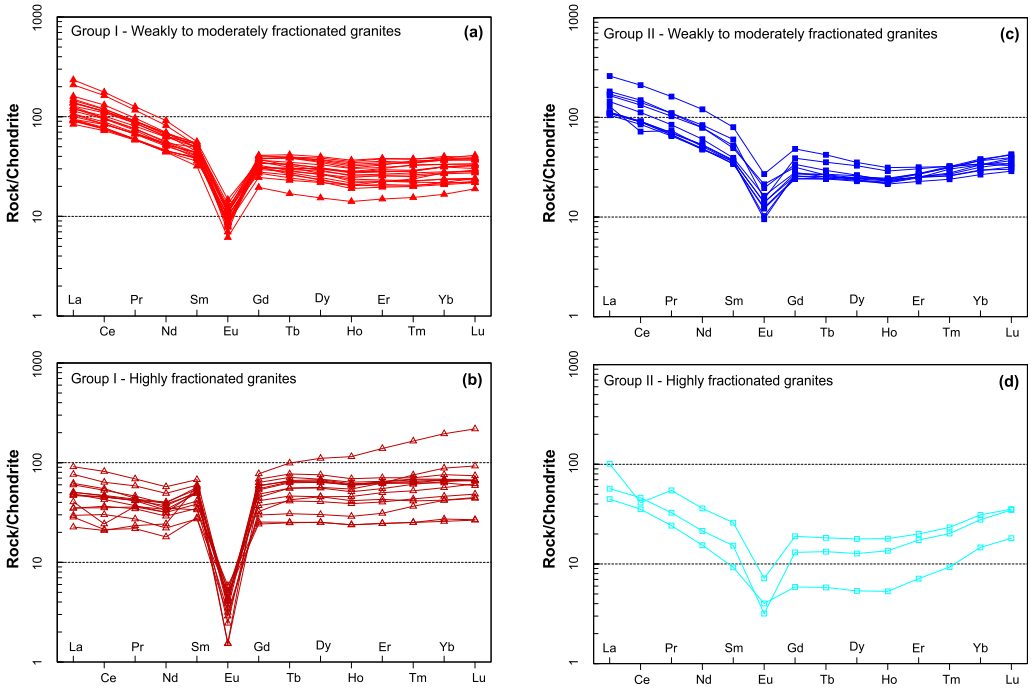

Fig. 5. (a) Chondrite normalized Rare Earth Elements (REE) patterns for: (a) weakly to moderately fractionated Group I granites; (b) highly fractionated Group I granites; (c) weakly to moderately fractionated Group II granites; (d) highly fractionated Group II granites. The chondrite values are from McDonough and Sun (1995).

Table 3
ID-TIMS U–Pb isotopic data on zircon from the Macao magmatic rocks.

Spot No.	Fraction analyzed	Weight (mg)	U (ppm)	Th/U	Pb_C (pg)	$^{206}Pb/^{204}Pb$[a]	$^{206}Pb/^{238}U$[b] age (Ma)	2σ abs	$^{207}Pb/^{235}U$[b] age (Ma)	2σ abs	$^{207}Pb/^{206}Pb$[b] age (Ma)	2σ abs	Rho concordia
C58 - Coarse-grained porphyritic biotite-microcline granite, Group I													
dwd6193	1 CA zr, ET535, Hf collected	0.0028	344	0.76	0.88	1832.57	164.19	0.19	165.06	0.51	177.54	5.74	0.818
dwd6183	1 CA zr, sl etched prism, ET535, Hf collected	0.0026	526	0.66	0.82	2766.73	163.12	0.23	164.91	0.45	190.69	4.43	0.844
dwd6195	1 CA zr, ET535	0.0026	825	0.52	0.79	4475.07	163.29	0.17	163.89	0.67	172.55	9.33	0.504
dwd6182	1 CA zr, etched spr, ET535, Hf collected	0.0027	948	0.39	1.12	3780.12	163.64	0.20	165.08	0.39	185.80	3.61	0.898
dwd6181	1 Ca zr, etched frag, ET535, Hf collected	0.0041	172	0.64	0.06	18323.30	166.39	0.47	182.61	1.78	398.04	21.23	0.511
dwd6194	1 CA zr, ET535	0.0025	366	0.86	1.01	1893.82	204.24	0.28	205.76	0.72	223.15	7.06	0.703
M18 - Fine- to medium-grained non-porphyritic garnet-bearing biotite-microcline granite, Group I													
dwd6202	1 CA zr, stubby unetched, Hf saved, ET535 spike	0.0017	657	0.59	1.74	1076.81	163.51	0.27	161.76	0.82	136.26	11.03	0.568
dwd6204	1 CA zr, stubby, crk, etched, ET535	0.0016	868	0.49	0.57	4015.59	163.61	0.19	164.01	0.52	169.80	6.44	0.714
dwd6205	1 CA zr, stubby, well etched, ET535	0.0015	870	0.62	0.48	4535.69	163.63	0.19	164.81	0.52	181.74	6.30	0.714
T17 - Coarse-grained non-porphyritic garnet-bearing biotite-microcline granite, Group I													
dwd6184	1 CA zr, etched stubby, ET535, Hf collected	0.0019	954	0.45	1.28	2329.98	161.50	0.21	161.44	0.63	160.57	8.10	0.670
dwd6198	1 CA zr, ET535	0.0008	813	0.57	0.67	1628.92	163.51	0.22	165.89	1.07	199.92	15.16	0.415
dwd6197	1 CA zr, ET535	0.0008	1032	0.58	0.62	2225.12	163.56	0.18	165.27	0.81	189.74	11.00	0.603
dwd6185	1 CA zr, etched tip, ET535, Hf collected	0.0012	651	0.63	2.20	606.54	163.68	0.26	162.91	2.41	151.69	34.74	0.725
dwd6196	1 CA zr, ET535, Hf collected	0.0012	448	0.54	1.18	773.42	163.97	0.22	168.21	0.75	228.27	9.02	0.737
dwd6186	1 CA zr	0.0019	403	0.82	46.57	46.87	172.64	3.63	192.53	56.08	443.83	786.55	0.028
M34 - Coarse-grained porphyritic biotite-orthoclase granite, Group II													
dwd6178	1 CA zr, tip, ET535, Hf collected	0.0061	548	0.44	0.85	6221.87	156.48	0.18	157.34	0.46	170.46	5.92	0.685
dwd6191	1 CA zr, ET535	0.0034	1313	0.50	0.93	7584.71	156.50	0.16	157.13	0.83	166.74	12.58	0.363
dwd6190	1 CA zr, ET535, Hf saved	0.0042	967	0.52	1.51	4261.53	156.55	0.18	156.98	0.57	163.38	7.81	0.589
dwd6180	1 CA zr, spr, ET535, Hf collected	0.0026	652	0.67	0.92	2931.87	156.64	0.20	157.06	0.73	163.36	10.18	0.609
dwd6179	1 CA zr, tip, ET535, Hf collected	0.0039	428	0.60	0.69	3841.56	156.85	0.24	158.11	0.62	177.05	8.20	0.609
T36 - Coarse-grained porphyritic biotite-orthoclase granite, Group II													
dwd6211	1 CA zr, stubby, melt incls, sl. etched, ET535 spike	0.0014	1590	0.61	0.60	5863.14	156.33	0.19	156.78	0.37	163.53	3.63	0.885
dwd6208	1 CA zr, stubby, melt incls, sl. etched, ET535 spike	0.0038	921	0.61	0.66	8392.12	156.52	0.19	156.73	0.34	159.80	2.93	0.936
dwd6207	1 CA zr, stubby, melt incls, sl. etched, ET535 spike	0.005	420	0.64	0.62	5354.31	156.60	0.18	156.92	0.50	161.79	6.50	0.690
dwd6209	1 CA zr, stubby, melt incls, sl. etched, ET535	0.0031	757	0.65	1.07	3491.92	156.61	0.17	156.86	0.44	160.64	5.44	0.765
dwd6206	1 CA zr, stubby, melt incls, sl. etched, ET535 spike	0.005	771	0.65	0.57	10778.09	156.76	0.17	157.14	0.39	162.95	4.58	0.787
dwd6210	1 CA zr, stubby, melt incls, sl. etched, ET535	0.0014	893	0.25	0.99	2118.53	164.53	0.22	164.57	0.80	165.05	10.76	0.580
C40 - Dacite dyke													
dwd6201	1 CA zr, ET535	0.0018	426	0.63	1.04	910.77	119.68	0.14	117.81	0.50	80.18	8.61	0.786
dwd6187	1 CA zr, etched, incls, spr	0.0024	355	0.80	2.03	542.44	123.71	0.20	125.28	0.83	155.14	14.54	0.620
dwd6200	1 CA zr, ET535	0.0022	230	0.83	0.62	1075.67	128.06	0.19	131.86	1.11	200.99	18.84	0.612
dwd6189	1 CA zr, stubby, incls, unetched, ET535, Hf collected	0.0016	423	0.45	0.85	1122.23	137.33	0.19	139.02	1.05	167.95	17.35	0.543
dwd6188	1 CA zr, etched, incls, spr	0.0023	794	0.40	0.64	3983.46	137.57	0.20	138.90	0.60	161.77	9.25	0.590
dwd6199	1 CA zr, ET535, Hf collected	0.0023	370	0.65	0.68	1965.71	153.34	0.21	154.19	0.83	167.33	11.85	0.596

Analyses are ordered from youngest to oldest $^{206}Pb/^{238}U$ age.
Weights are based on estimates from microphotographs.
Number of grains analyzed is at beginning of the "Fraction analyzed" column.
Abbreviations: CA–chemically abraded, ZR–zircon, INCLS–inclusions, EQ–equant, SPR–short prismatic, LPR–long prismatic, CRK–cracked, FRAG–fragmented, SL–slightly.
Th/U: calculated from radiogenic $^{208}Pb/^{206}Pb$ ratio and $^{206}Pb/^{238}U$ age assuming concordance.
Pb_C: common Pb assuming the isotopic composition of lab blank: $^{206}Pb/^{204}Pb$=18.221; $^{207}Pb/^{204}Pb$=15.612; $^{208}Pb/^{204}Pb$=39.360 (2% error).
Uranium decay constants: L238 = 1.55125×10^{-4}/Ma, L235 = 938485×10^{-4}/Ma (Jaffey et al., 1971).
Concordia coordinates: Y = $^{206}Pb/^{238}U$ = EXP(L238 × (206-238 Age)) - 1; X = $^{207}Pb/^{235}U$ = EXP(L235 × (207-235 Age)) - 1.
$^{207}Pb/^{206}Pb$ = X/(137.88 × Y); Rho: Error correlation coefficient for concordia coordinates.
[a] $^{206}Pb/^{204}Pb$ are measured values corrected for fractionation and spike.
[b] $^{206}Pb/^{238}U$ age, $^{207}Pb/^{235}U$ age and $^{207}Pb/^{206}Pb$ age are corrected for common Pb assuming laboratory blank composition and ^{230}Th disequilibrium assuming a magmatic Th/U of 4.2.

$^{206}Pb/^{238}U$ age. Significant scatter to the right is probably due to Precambrian inheritance.

Zircon separates from many of the granitic rocks are bimodal with a population of fresh grains and another of strongly altered and cracked crystals (see Supplementary File 3). In some instances, altered/cracked zircons may overgrow the population of fresh euhedral grains. Only fresh grains were dated even when the zircon population was dominated by the altered type.

Samples M18, T17 (Group I granites) generally produced overlapping $^{206}Pb/^{238}U$ ages for individual grains, although T17 also yielded a grain with an age that is 2 Ma younger than the main cluster (Fig. 7c) and another Group I sample (C58, Fig. 7a) produced data that scatter outside of error, at least in part due to Mesozoic and Archean inheritance. Ten out of fifteen grains from Group I define an age of 163.5 ± 0.2 Ma although with a large MSWD of 4.5. Group II granite samples T36 and M34 (Fig. 7d and e, respectively) mostly scatter only slightly outside of error. Nine out of eleven grains from Group II define an age of 156.6 ± 0.1 Ma with an MSWD of 1.7. A single older 164.5 Ma grain (Table 3) may represent an antecryst acquired from Group I. Zircon in the dacite dyke (sample C40) appears to be almost entirely inherited with a span of younger near-concordant ages from 120 Ma to 153 Ma.

Though zircon grains were chosen based on chemical and morphological criteria for determination of crystallization ages of the magmatic rocks, inheritance could not be avoided in some cases. The analysis with the oldest concordant $^{206}Pb/^{238}U$ age indicates an inherited Phanerozoic source that is at least 205 Ma old (Fig. 7a). The oldest discordant analysis (from sample C58) suggests an inherited Mesoarchean age (ca. 3.5 Ga; Fig. 7a).

4.4. LA-MC-ICPMS geochronology

Thirteen samples were analyzed for U–Pb zircon geochronology using the LA-MC-ICPMS method (Table 4 and Supplementary File 4,

Table 4
Summary of LA-MC-ICPMS and ID-TIMS dating.

LA-MC-ICPMS dating				
Group I samples	Avg. age (Ma)	95% conf.	MSWD	N
T22	162.91	0.73	0.8	12
C64	163.34	0.50	1.7	28
T33	163.79	0.53	1.5	19
C05old	163.60	0.64	0.3	15
C33	164.23	0.90	2.6	15
C66	163.87	0.70	1.6	20
T43	164.28	0.86	2.1	12
C68	164.47	0.61	1.9	20
Avg.	163.75	0.42	2.4	8
Group II samples				
C05yng	155.48	0.82	1.6	13
M35	155.86	0.56	1.5	22
M19	156.34	0.33	0.8	35
M29	156.44	0.61	0.6	15
T36	156.05	0.52	1.5	19
Avg.	156.16	0.38	1.5	5
Dacite dyke				
T49	150.64	0.55	1.15	10

ID-TIMS dating				
Group I samples	Avg. age (Ma)	2σ	MSWD	N
M18	163.60	0.12	0.3	3
T17	163.67	0.32	3.5	4
C58	163.36	0.61	6.2	3
Avg.	163.54	0.16	4.5	10
Group II samples				
M34	156.53	0.16	0.1	4
T36	156.57	0.19	2.9	5
Avg.	156.56	0.10	1.7	9
Dacite dyke				
C40	<119.68	0.14	-	1

Abbreviations: Avg.—average; old—older zircon population; yng—younger zircon population; conf.—confidence; MSWD—Mean square weighted deviation.

Figs. 8 and 9; see also Supplementary File 2 for details on the location and general characteristics of the analyzed samples). Off-line data reduction was performed by the software ICPMSDataCal. Version 8.0 (Liu et al., 2009). No common Pb has been corrected. All reported ages were calculated using the Isoplot program (Ludwig, 1998, 2012). Individual analyses in the data table (Supplementary File 4) and concordia plots are presented as 1σ absolute error and uncertainties in average ages are given at the 95% level (2σ). As was done for ID-TIMS results, $^{206}Pb/^{238}U$ ages were calculated and used in the following discussion.

The zircons chosen for these analyses are subhedral to euhedral with pyramidal and prismatic shape, 80–200 μm long, with length-to-width ratios of 2:1 to 5:1. Representative zircon BSE images (Figs. 6 and 8) show that most grains are internally homogeneous or have oscillatory zoning, which is indicative of a magmatic origin (Rubatto and Gebauer, 2000), with a minority of grains exhibiting inherited cores and magmatic rims.

The zircons of the less fractionated granites (Zr/Hf > 25) are usually transparent, euhedral, colorless to pale yellow in color. Some appear brownish due to radiation damage from high U content, with the number of this type of grains tending to increase with increasing degree of evolution (e.g., Zr/Hf ratio). These metamict zircons generally have a lower refractive index compared with non-damaged zircons. Some of the most fractionated samples (Zr/Hf ≤ 25) still preserve a small population of fresh zircons that could provide crystallization age results, while others could not be dated as the whole population of zircon grains was altered and therefore subject to significant Pb loss. Many zircons from these highly fractionated samples have mineral inclusions, such as REE phosphate phases and calcite (see Supplementary File 3 for more details), which were avoided to prevent inaccurate age results.

The zircon U–Pb ages obtained by LA-MC-ICPMS for the granitic rocks are presented in detail in Supplementary File 4 and summarized in Table 4. Except for obvious inheritance, they form two groups with average ages of 163.8 ± 0.4 Ma and 156.2 ± 0.4 Ma. Sample C05 (Fig. 9a) seems to contain two populations of zircons representative of each of those two periods. The Taipa dacite dyke yields a relatively young age of ~150 Ma, although still older than the Coloane dacite dyke dated by ID-TIMS (<119.68 ± 0.14 Ma, Fig. 7f).

Although most of the zircon grains crystallized from granitic magmas, some of the grains revealed inheritance (see Fig. 9). The oldest concordant inherited age obtained was 2407 Ma (Paleo-Proterozoic), although several more recent Proterozoic and Paleozoic concordant ages were also obtained.

To verify the agreement between ID-TIMS and LA-MC-ICPMS data, sample T36 was dated by both methods yielding similar ages within error (156.05 ± 0.52 Ma for LA-MC-ICPMS and 156.6 ± 0.19 Ma for ID-TIMS).

5. Discussion

5.1. Multistage emplacement of Macao granites

The analyzed samples provide a robust dataset for geochronological characterization of this region of SE Asia, adding significantly to existing data.

In previous works on the geology of Macao (Ribeiro et al., 1992, 2010), K–Ar Jurassic ages of 154 ± 5 Ma to 168 ± 4 Ma were reported, which are, within error, similar to the ages obtained in this study (see Tables 3 and 4 and Supplementary File 4). An age of 94 ± 2 Ma was also reported by those authors for one granite from Coloane, which led them to suggest the existence of Upper Cretaceous granites in Macao. Despite the large number of age determinations performed in this study, no age similar to that was obtained.

Although Late Cretaceous magmatism is known to have affected SE China during the second period of the Yanshanian orogeny (e.g., Chen et al., 2008; Xu et al., 2015; Zhao et al., 2015, 2016; Yan et al., 2017; Zheng et al., 2017b), no studies have been found mentioning ~90 Ma granitic rocks outcropping in areas adjacent to Macao. In Hong Kong, the more recent pulse occurred around 140.8 ± 0.6 Ma (Sewell et al., 2012). Moreover, considering that the sample dated by Ribeiro et al. (1992) is a non-porphyritic fine-grained garnet-bearing biotite-microcline granite, with the same petrographic and geochemical characteristics as the highly fractionated samples of the ca. 163.5 Ma Group I granites from this study, we assume that the 94 ± 2 Ma age results from loss of Ar. In fact, this sample was collected near an important fault zone in the easternmost area of Coloane; such setting may have allowed hydrothermal fluid circulation to damage the biotite from adjacent granites. This age may thus hypothetically indicate the time of an important movement of that fault during the Late Cretaceous. Similar isotope resetting situations have been observed in SE Asia, where granites of now known Jurassic age were previously considered to be Cretaceous using the K/Ar method (Bignell and Snelling, 1977; Beckinsale, 1979; Cobbing, 2000). Taking all these into account, the existence of Cretaceous granites will not be considered in the next discussion, which will be based on U–Pb zircon geochronological analyses.

The U–Pb geochronological data presented in this study allow us to assign distinct ages to the two granite groups (I and II), as

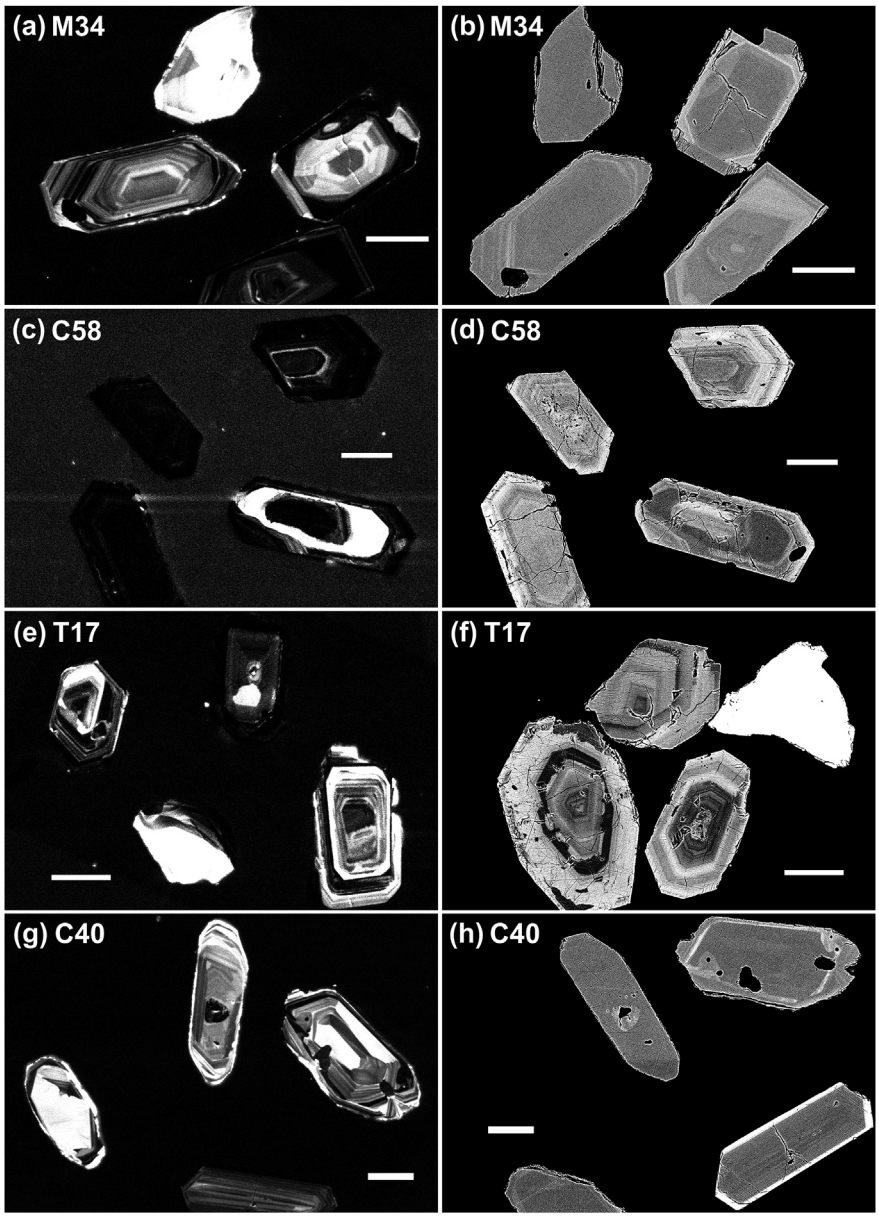

Fig. 6. Backscattered Electron (BSE) and cathodoluminescence (CL) images of representative zircons from Macao samples analyzed by ID-TIMS. The scale bar represents 50 μm.

initially anticipated on the basis of petrographic characteristics (see section 4.1 Petrography; see also below).

LA-MC-ICPMS average ages of 163.8 ± 0.4 Ma and 156.2 ± 0.4 Ma overlap with the respective ages for groups I and II determined by ID-TIMS: 163.5 ± 0.2 Ma and 156.6 ± 0.1 Ma (see Table 4). The individual analyses from LA-MC-ICPMS generally scatter within error of the average. This is not the case for the more precise ID-TIMS data, which shows significant scatter, especially for the Group I zircons. This may be due to the ID-TIMS errors being smaller than the time span for crystallization of zircon within the granitic complexes. Crystallization is unlikely to occur within a magma chamber, but rather within a fluctuating zone of partial melt that may retain small proportions of magma for several million years (Bachmann and Bergantz, 2008; Frazer et al., 2014). A single zircon grain may thus display a range of ages, or zircon that crystallized during an early phase of partial melting may become incorporated into a later phase. Sample C05 contains populations of zircon from Group I and Group II events and was therefore apparently subject to crystallization during both. The earliest Group I magmatism appears to have been more susceptible to picking up inheritance than the later Group II magmas.

The exceptionally tightly constrained record of Mesozoic plutonic activity in Macao provided by this study suggests a multistage granite emplacement in this relatively small area. Indeed the results obtained for sixteen samples point to the existence of two periods of granitic emplacement: Group I – 164.5 ± 0.6 Ma to 162.9 ± 0.7 Ma; Group II – 156.6 ± 0.2 Ma to 155.5 ± 0.8 Ma. The average age of eight dated samples from Group I is 163.75 ± 0.42 Ma (MSWD = 2.4) while that of the four dated samples from Group II is 156.16 ± 0.38 Ma (MSWD = 1.5). The scatter of individual ages suggests that both groups may have been emplaced over a noticeable, although barely resolvable, age range. Probability density plots (Ludwig, 2012) for both groups are shown in Fig. 10. These are based on the summation of average ages, not individual U–Pb analyses, so that each sample age has equal weight. Both populations are somewhat asymmetrical suggesting a

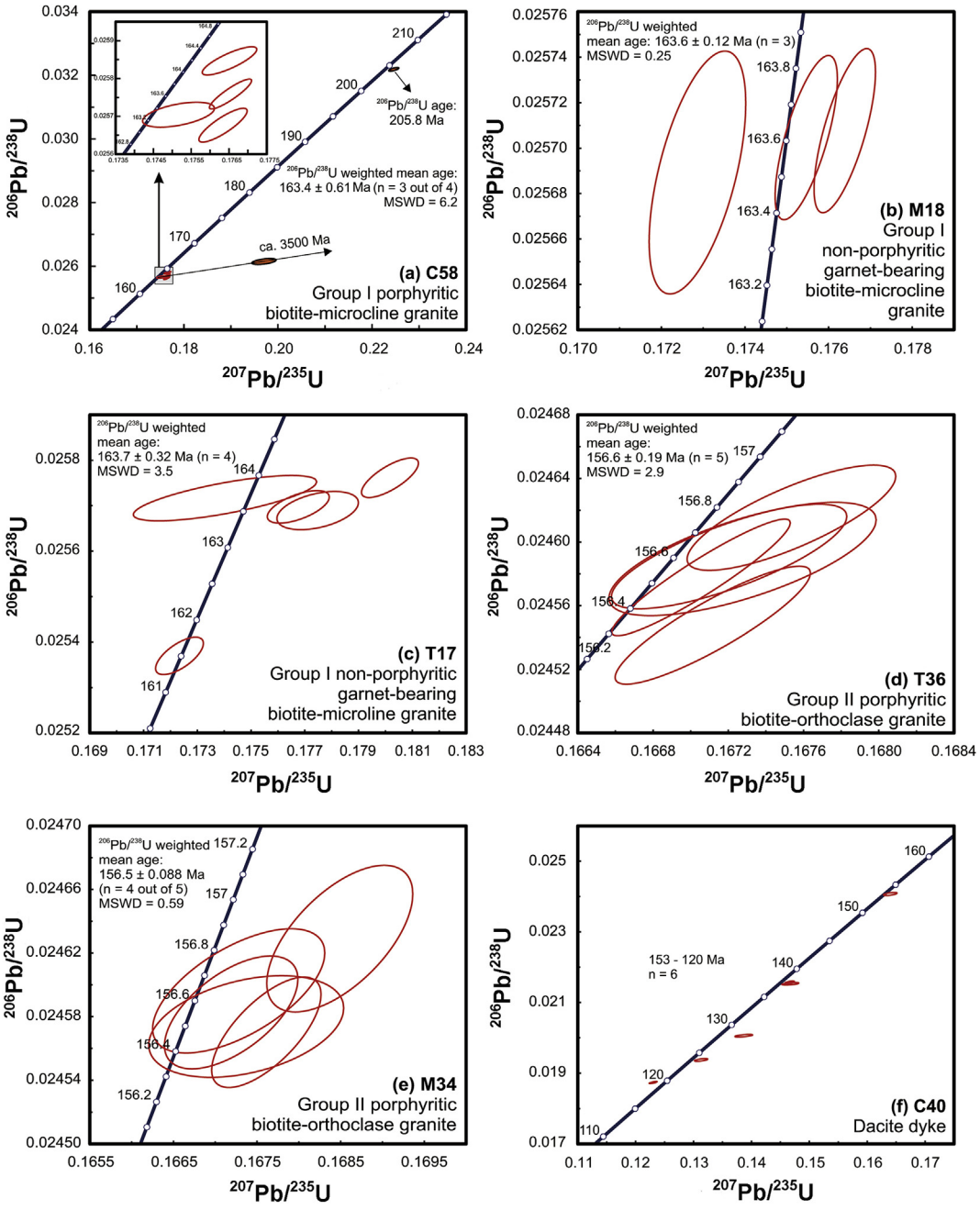

Fig. 7. Zircon U–Pb concordia diagrams for Macao samples dated by ID-TIMS: (a–e) granites and (f) dacite dyke.

slightly older component in Group I and a slightly younger one in Group II. Applying the unmixing algorithm of Sambridge and Compston (1994) using Isoplot, and assuming only two components, yields ages that differ by about 0.9 ± 0.6 Ma for Group I and about 0.35 ± 0.8 Ma for Group II (Fig. 10). The estimate for Group II is within error and that for Group I barely outside of error. However, a two-age approximation is likely to give a minimum estimate. Given that each of the pluton ages represents the average of a significant number of measurements, it should be valid to take the difference between the oldest and youngest average age, which is 1.6 ± 0.9 Ma for Group I and 1.1 ± 0.8 Ma for Group II. As these are 2σ errors, the differences are non-zero outside of error. The Group I and II magmatic periods were separated by a much longer, ca. 6 Ma, period of quiescence. Considering that the crystallization of zircons may span 10^4 to 10^6 years in magmatic systems (Charlier et al., 2005; Matzel et al., 2006; Bachman et al., 2007; Memeti et al., 2010; Schoene et al., 2012; Barboni et al., 2013; Keller et al., 2018), it is important to evaluate if the two clusters of dates identified correspond to two geochemically distinct groups of granites. With this purpose, a comparison of some characteristics of rocks of each of those groups is made below.

The structure of K-feldspar crystals of each group is different. Group I is marked by the presence of microcline (Fig. 3a and c) while Group II contains orthoclase (Fig. 3e), easily distinguishable in hand specimen by the grey whitish color of the first as opposed to the pinkish color of orthoclase and also, under microscope, by different types of twinning (albite/pericline vs. Carlsbad, respectively; Fig. 3b). While orthoclase is monoclinic and stable at

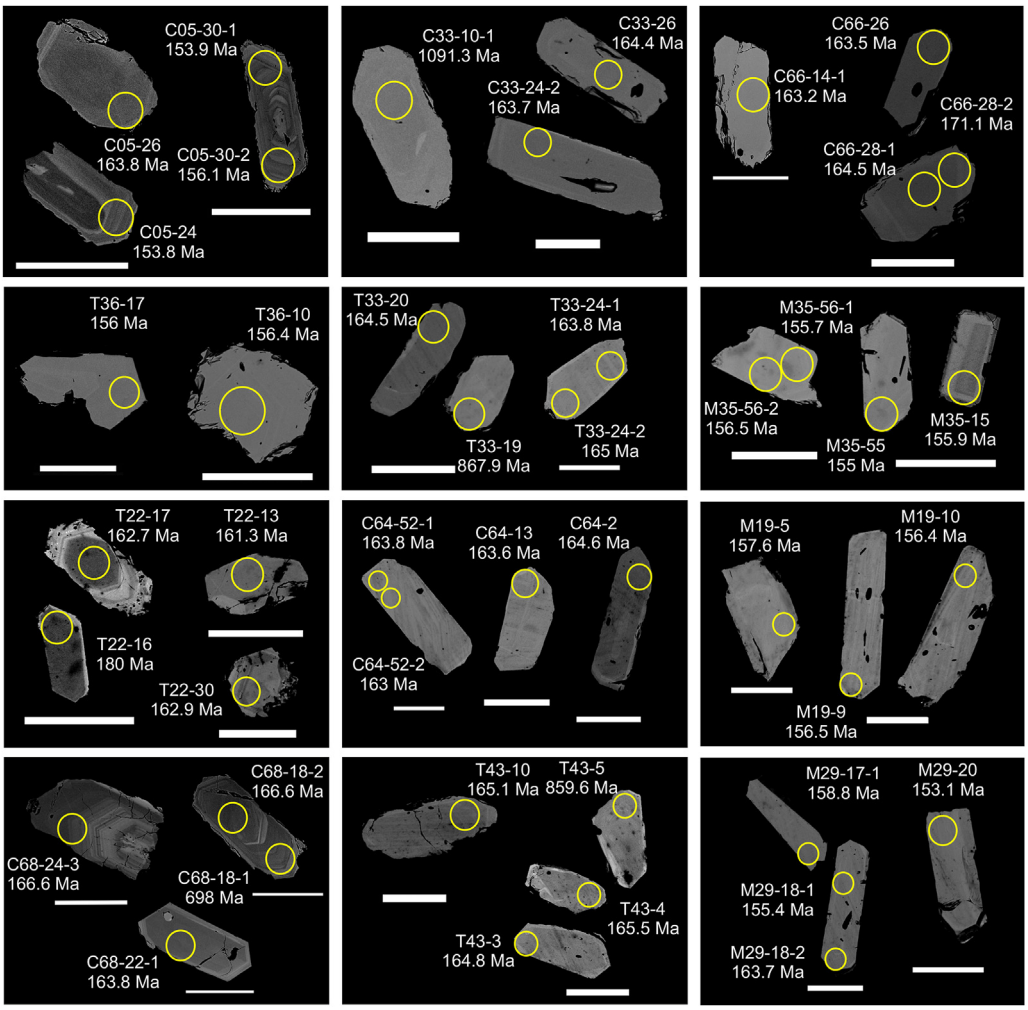

Fig. 8. Backscattered Electron (BSE) images of representative zircons from Macao samples analyzed with LA-MC-ICPMS. The yellow circles represent the laser spot, the corresponding age also being shown. The scale bar represents 100 μm.

temperatures between 500 °C and 900 °C, microcline is a triclinic low-temperature K-feldspar stable at temperatures below than 500 °C (Smith and Brown, 1974; Deer et al., 1992). It is generally accepted that microcline rarely crystallizes directly from magma, and is formed typically by inversion of an earlier monoclinic K-felsdspar phase or, in some cases, by ion exchange and recrystallization of sodic plagioclase to microcline ± muscovite (Smith and Brown, 1974; Blasi et al., 1984; Collins, 2000). Since no evidence for pervasive K-metasomatic processes in the studied samples of Group I granites was found, the last hypothesis is unlikely. The ordering of K-feldspars can be linked to the cooling rates of magmas (e.g., Horvat, 2011), which could suggest a slower cooling rate for Group I relatively to the later Group II magmas thus providing temporal conditions for the inversion of monoclinic K-feldspar (orthoclase) to triclinic K-feldspar (microcline). However, considering that both groups occur in a small area (30 km^2) at similar altitude, it is probable that they were emplaced at identical depths. This and the fact that Group I granites are only ca. 6 Ma older than Group II granites, makes difficult that magmas from Group II could have cooled much faster than those of Group I. As reported above (see section 4.1), Group I granites are clearly more deformed than Group II granites, suggesting that, in Macao, deformation acted as an external mechanism in the monoclinic-triclinic transition, as proposed, for example, by Bell and Johnson (1989) and Vernon and Patterson (2002) for microcline occurrences elsewhere.

Subtle differences can also be identified in the accessory phases. Titanite is an abundant accessory phase in Group II granites, occurring as well-developed euhedral lozenge-shaped crystals (Fig. 3f), but tends to be rare and poorly developed in Group I. With increasing degree of differentiation, the porphyritic character tends to become less prominent in both groups until it is totally unrecognizable in the most fractionated rocks (fine-grained granites and microgranite and aplite dykes). However, the highly fractionated granites of Group I are marked by the presence of spessartine-rich garnet as accessory mineral (Fig. 3d), which is absent in Group II granites.

The MMEs of the two groups also differ in texture and mineralogy. MMEs in Group I granites (Fig. 3h and i) usually have bigger dimensions (up to 1 m in diameter), granodiorite composition, acicular biotite and no accessory titanite. MMEs in Group II granites (Fig. 3j and k) on the other hand, have smaller dimensions (centimeter to decimeter-wide), quartz monzodioritic compositions, lozenge-shaped biotite, abundant titanite and in some cases hornblende.

Biotite is the dominant ferromagnesian mineral in Macao granitic rocks. Although the chemical compositions of biotites from both groups overlap for most elements, differences can be observed for specific elements such as Mg (Fig. 4c), Ti (Fig. 4d) and Al (Fig. 4a and d). Apart from some Mn-rich biotite flakes (Fig. 4c), the biotites from Group I granites have Mg = 0.08–1.69 apfu, Ti = 0.11–0.40

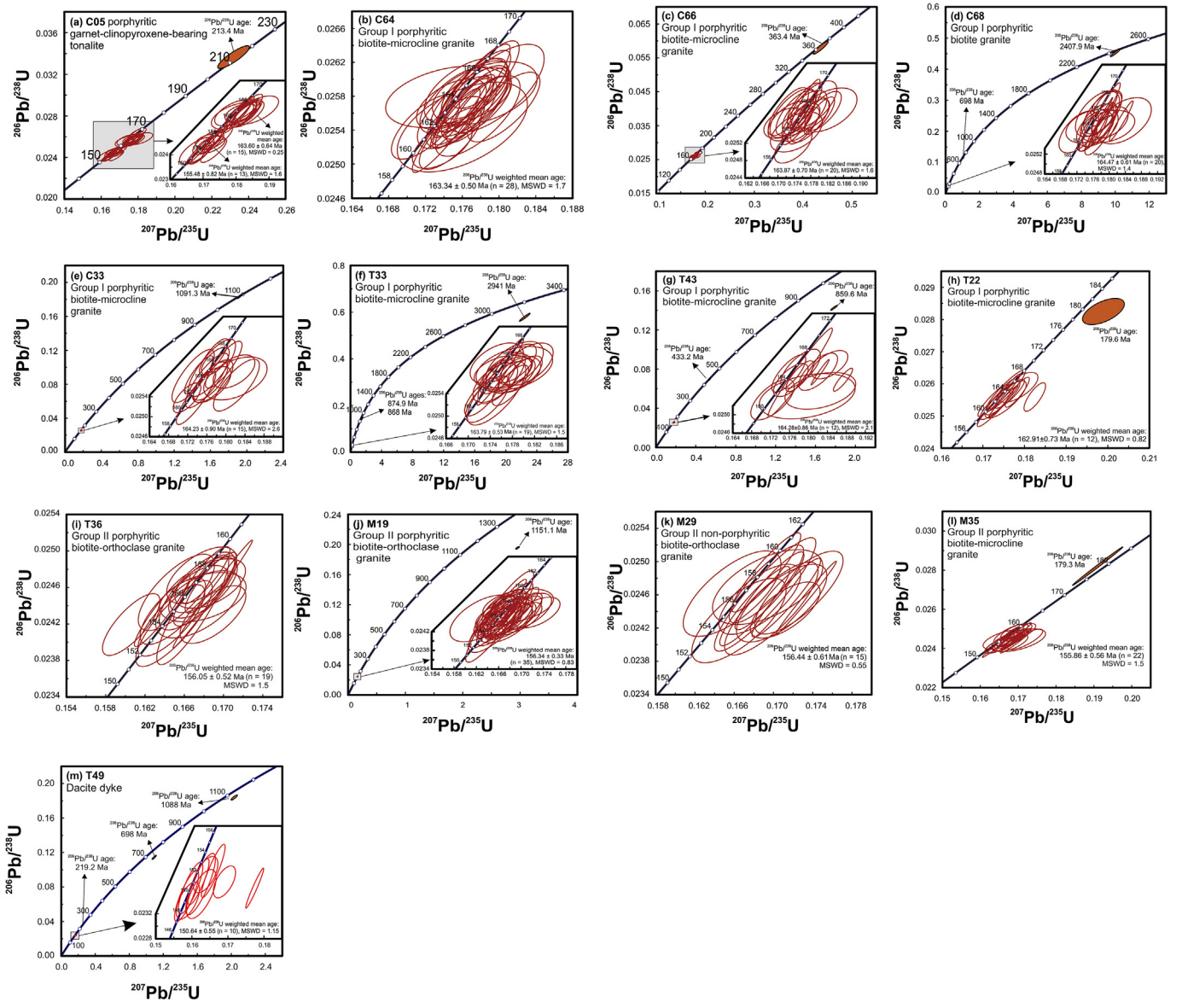

Fig. 9. Zircon U–Pb concordia diagrams for Macao samples dated by LA-MC-ICPMS: (a–l) granites and (m) dacite dyke.

apfu and Al^{vi} = 0.30–1.34 apfu, whereas those from Group II granites are characterized by comparatively higher Mg = 1.36–2.22 apfu, higher Ti = 0.31–0.5 apfu and lower Al^{vi} < 0.48 apfu. The higher Ti contents of biotites from Group II granites (Fig. 4d) are consistent with more abundant and well-developed titanite in these rocks. Considering the biotite tendency to reflect magmatic physico-chemical conditions (e.g., Wones and Eugster, 1965; Nachit et al., 1985, 2005; Abdel-Rahman, 1994; Bónová et al., 2010; Esmaeily et al., 2013), the chemistry of biotites from the studied samples reinforces the existence of two chemically distinct groups.

REE whole-rock compositions of different lithofacies from the two groups follow different evolutionary trends with increasing differentiation, suggesting distinct fractional crystallization paths. Though the less fractionated types of both groups display moderately fractionated REE patterns [$(La/Yb)_N$ = 2.41–10.76] and Eu negative anomalies (Fig. 5a and c), the REE patterns of the highly fractionated types clearly differ. In Group I (Fig. 5b) the REE patterns are flat to slightly upward [$(La/Yb)_N$ = 0.12–1.2] and have well-pronounced Eu anomalies (Eu/Eu* = 0.02–0.19), with some samples showing evidence for the M-type tetrad effect ($TE_{1,3}$ up to 1.13) as defined by Irber (1999) (see also footnotes of Table 2). The flat shape of Group I REE patterns suggests fractionation of light REE-bearing phases such as allanite and monazite. On the other hand, Group II (Fig. 5d) REE patterns are concave upwards with comparatively smaller Eu anomalies (Eu/Eu* = 0.23–0.54) and are characterized by the absence of the tetrad effect. The concave upwards shape of Group II REE patterns could be achieved through higher fractionation percentages of middle REE-compatible minerals such as apatite and/or titanite. The two groups also show distinguishable evolutionary trends on diagrams involving ratios between REE (Fig. 11).

In conclusion, the mineralogical and whole-rock geochemical characteristics support the existence of two chemically distinct groups of granites in Macao, which, judging by the ages presented in this study, were emplaced in two pulses during the Upper Jurassic.

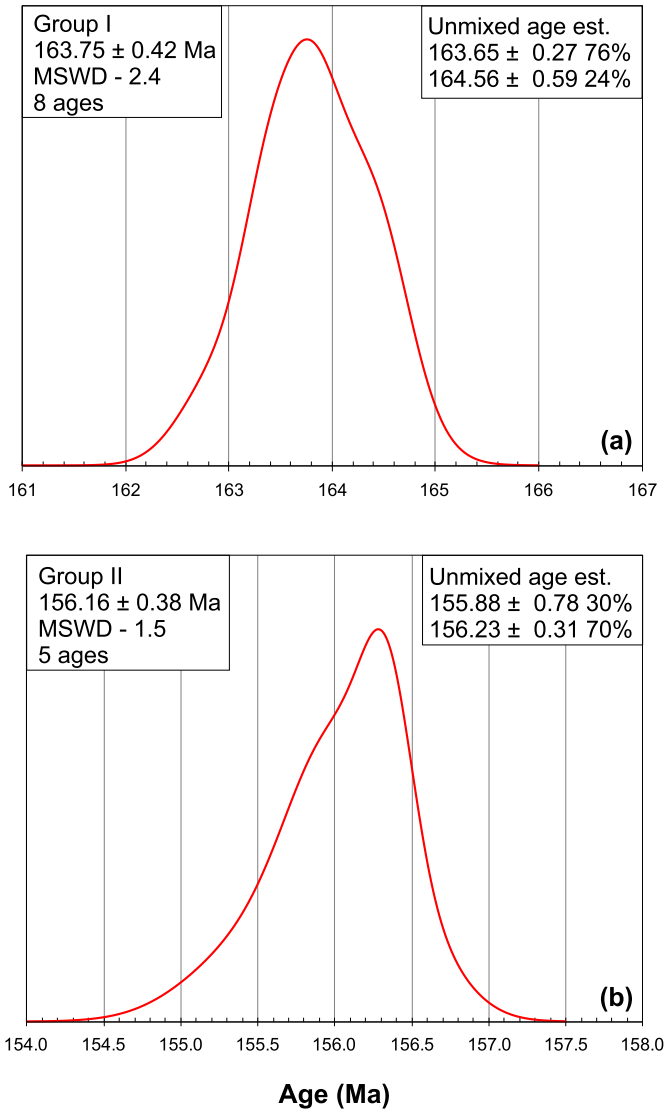

Fig. 10. Probability density distributions for: (a) eight zircon ages measured from Group I populations and (b) five ages measured on Group II zircon populations. Also shown are best estimates for unmixing of two ages from each curve as discussed in the text.

5.2. Inheritance ages

The age spectra for inherited zircons from granites can be a useful tool to obtain insights on the age of potential protoliths (Keay et al., 1999). However, the number of analyses of inherited zircon grains in the present study was not sufficient to identify significant inherited age populations. This is in part due to the fact that most of the Macao granites are metaluminous to weakly peraluminous (A/CNK = 0.96–1.13), which are typically inheritance-poor, in contrast with what has been usually observed for highly peraluminous granites (Miller et al., 2003, 2007; see also Watson and Harrison, 1983). Moreover, many of the zircon grains were strongly altered (see sections 3.2.2. and 3.2.3) and consequently the achievement of accurate results was not possible in these cases.

Most of analyzed inherited zircon grains or cores were extracted from Group I granites, while samples from Group II contain little or no inheritance making it impossible to draw conclusions on the differences of the involved magmatic sources in both periods. Zircon inheritance ages obtained from both methodologies suggest a wide range of Phanerozoic and Precambrian sources (Fig. 12). Since long-lived felsic magmatic systems may be highly complex, made up of several inputs of magma, not all such zircon crystals in a particular rock need have crystallized from the same pulse or increment of melt (Miller et al., 2007). Thus, the occurrence of antecrysts, that were crystallized from an earlier magmatic pulse and were later incorporated in a subsequent pulse(s), is common in these magmatic systems. This is probably the case for the range of inherited ages between 165–180 Ma (see Supplementary File 4 and Fig. 12). Many of the older inherited grains (>180 Ma) are probably xenocrystic in origin, belonging to wall rock assimilated during ascent and emplacement of the granitic magmas, or representing residual zircons inherited from the magma source.

The oldest concordant inherited age found in this study is a $^{206}Pb/^{238}U$ age of 2407 Ma, suggesting that the source of the Macao granites might be as old as Paleo-Proterozoic. However, a less concordant (91%) $^{206}Pb/^{238}U$ age of 2941 Ma obtained for sample T33 means that an Archean component cannot be ruled out. This is in agreement with studies on crustal xenoliths and zircon xenocrysts entrained in Mesozoic and Cenozoic volcanic rocks from neighboring areas, suggesting the existence of a highly evolved Archean–Paleoproterozoic basement beneath the western Cathaysia Block (Zheng et al., 2011; Li et al., 2018).

5.3. Macao granitic magmatism in the SE China context

It is well known that a major magmatic event took place in a vast area of SE China between 165 and 140 Ma (e.g., Sewell et al., 1992; Zhou and Li, 2000; Li et al., 2004, 2007; Guo et al., 2012; Huang et al., 2013; Zhang et al., 2015; Chen et al., 2017). Among the igneous rocks formed during this time span, strongly metaluminous to weakly-peraluminous biotite monzogranites are predominant (e.g., Sewell et al., 1992; Li et al., 2007; Huang et al., 2013; Zhang et al., 2015), associated with minor gabbros, basalts, syenites, peraluminous granites and A-type granites (e.g., Li et al., 2003, 2004, 2007; Xu et al., 2007; Wang et al., 2008; He et al., 2010; Meng et al., 2012; Zhang et al., 2017). On the other hand, high precision U–Pb zircon ages published for the neighboring region of Hong Kong (Sewell et al., 2012; see also; Sewell et al., 1992) enabled the identification of four main magmatic pulses: (1) 165–160 Ma (Lamma Suite); (2) 148–146 Ma (Kwai Chung Suite); (3) 143 Ma (Cheung Chau Suite) and; (4) 141 Ma (Lion Rock Suite). Based on inherited zircon ages from subsequent Hong Kong pulses and a date from a rhyolite dyke, Sewell et al. (2012) suggested the existence of a more localized magmatic event in Hong Kong region ca. 152 Ma ago.

This study demonstrates that granitic magmatism in the Macao territory, some 50 km from Hong Kong, was emplaced as two pulses occurring between 164.5 ± 0.6 Ma and 162.9 ± 0.7 Ma (Group I) and between 156.6 ± 0.2 Ma and 155.5 ± 0.8 Ma (Group II). These two periods of granitic magmatism in Macao can be integrated into the major magmatic event recorded in SE China (see above), the Group I granites being coeval with the Lamma Suite of Hong Kong, whereas no counterparts of the Group II have been identified (see Fig. 13). Our data for the Macao Group II granites indicate the occurrence in the Pearl River Delta region (southern coast of Guangdong province) of another granitic pulse in addition to those proposed by Swell et al. (2012) based on the study of the Hong Kong region.

Considering the existence in Macao of two distinct but proximal granitic pulses spanning about 9 Ma, we suggest that the Macao granitic suite was incrementally assembled, as proposed by Coleman et al. (2004) for a Californian intrusive suite (see also Glazner et al., 2004; Annen, 2011; Menand et al., 2015). Such incremental growth of granitic plutonism in the region is also shown

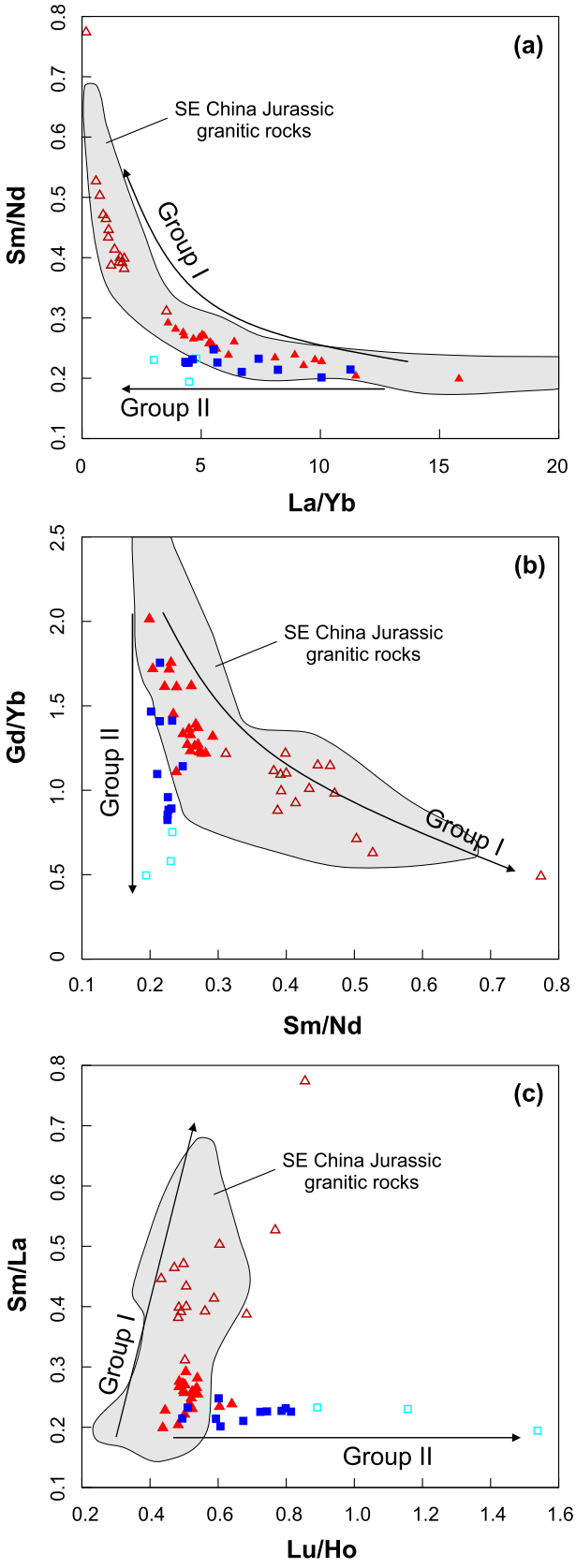

Fig. 11. REE ratios variation diagrams for the Macao granites. (a) Sm/Nd vs. La/Yb; (b) Gd/Yb vs. Sm/Nd; (c) Sm/La vs. Lu/Ho. Arrows represent the distinct evolutionary trends followed by the two groups. The gray area contains data from Jurassic (160–150 Ma) granitic rocks from SE China (Li et al., 2007; Huang et al., 2012, 2015; Zhang et al., 2015, 2017; Qiu et al., 2016; Jiang and Zhu, 2017; Jiang et al., 2018).

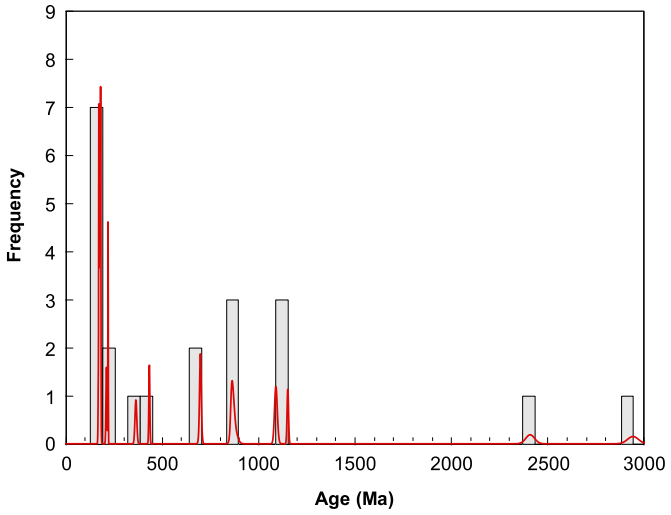

Fig. 12. Frequency plot of inherited ages of zircons from the Macao magmatic rocks.

by the existence in Hong Kong of several granitic pulses spanning in time for approximately 24 Ma.

It is noteworthy that the Macao Jurassic granites are mostly biotite monzogranites as in other areas of SE China. In this study, key differences in petrography, mineralogy and geochemistry have been shown to exist between the two pulses. This suggests that the same type of temporal-related mineralogical and chemical variations may exist in other granitic regions of SE China. The knowledge of such variations could help correlate different areas and constrain the spatial-temporal distribution of individual magma pulses on a regional scale. The understanding of the petrogenetic causes of such differences might yield important clues to better explain the still controversial Jurassic–Cretaceous granitic magmatism in the Cathaysia Block (SE China).

However, we emphasize that most of the studies have regarded these rocks as the result of a single magmatic event rather than discrete pulses with distinct compositional characteristics (e.g., Li et al., 2007; Huang et al., 2012; Zhang et al., 2015, 2017; Qiu et al., 2016; Jiang and Zhu, 2017; Jiang et al., 2018). Indeed, a peak of magmatic activity in SE China took place around 165–150 Ma during the Early Yanshanian orogeny (Fig. 13; Zhou et al., 2006; Li et al., 2007). When comparing REE data of the Macao granites with Jurassic granites (165–150 Ma) from nearby areas in SE China, it is clear that the Macao Group I granites and the SE China granites follow a similar evolutionary trend (Fig. 11). In contrast, the Macao Group II granites follow a distinct evolutionary path marked by relatively constant Sm/Nd ratios and increasing Lu/Ho ratios (Fig. 11c). Therefore, either the latter group has not been identified in other areas of SE China or it may represent a more localized magmatic pulse, which outcrops only in Macao and possibly in its close surroundings. However, regarding ages, both groups fall within the Jurassic magmatic peak (Fig. 13), and therefore are likely to have been formed in the same tectonic setting. We thus propose that, rather than a significant change in tectonic setting, the observed petrographic and compositional differences between Group I and Group II granites were caused by different magmatic evolution processes.

The ages obtained for dacite dykes (Taipa: 150.64 ± 0.55 Ma; Coloane: <120 Ma) clearly differ from those obtained for the granitic rocks. The Coloane dacite is distinctly younger than the youngest ages obtained in Hong Kong, which date back to around 140 Ma (Davis et al., 1997; Campbell et al., 2007; Sewell et al., 2012). Despite the fact that most of the magmatic activity in Macao

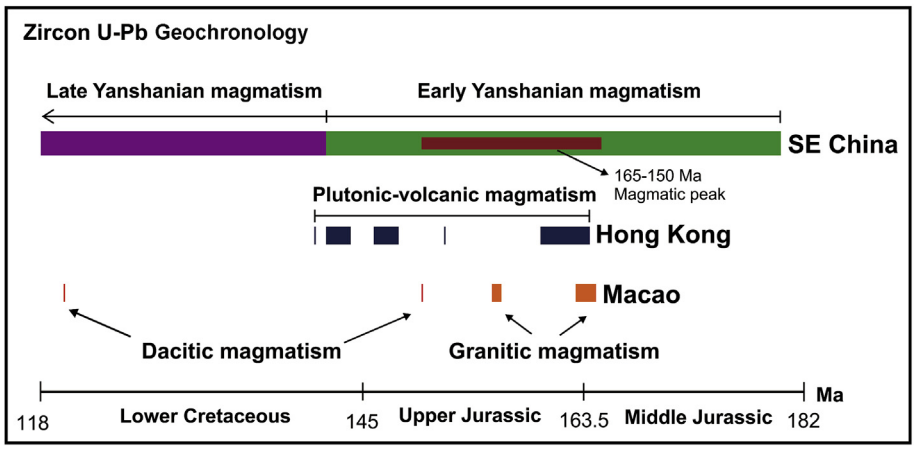

Fig. 13. Scheme showing the timing of magmatic pulses in Macao (this study) and Hong Kong (Sewell et al., 2012) territories, plus the Early and Late Yanshanian periods (Zhou et al., 2006) and the 160–150 Ma magmatic peak in SE China (Li et al., 2007; Huang et al., 2012, 2015; Zhang et al., 2015, 2017; Qiu et al., 2016; Jiang and Zhu, 2017; Jiang et al., 2018).

happened during the Early Yanshanian period, the age of the younger dacite dyke indicates that the territory was also affected, though to a lesser extent, by Late Yanshanian magmatism.

It is not a central objective of this paper to discuss the origin of the studied rocks. However, we note that the change in the type of magmatism in Macao from granitic to dacitic is likely to correspond to a change in the regional tectonic regime inducing a significant change on the magma genesis processes. The origin of Jurassic granites in SE China has been associated to an extensional regime coeval with foundering of the subducting paleo-Pacific plate, leading to asthenosphere upwelling and high crustal geothermal gradients required for granite genesis (e.g., Li et al., 2007; Li and Li, 2007; Huang et al., 2012, 2015; Sewell et al., 2016). On the other hand, the Macao dacite dykes are characterized by high LILE/HFSE ratios (e.g., $(Rb/La)_N = 3.8–8.5$) and negative anomalies of Nb, Ta and Ti ($Ti/Ti^* up to 1.12$). Though the dacites may have suffered some degree of crustal contamination as indicated by the presence of inherited zircons, these elemental characteristics are also identical to those characterizing arc-like subduction-related magmas (e.g., Kelemen and Hanghøj, 2003; Hürlimann et al., 2016). The Macao dacites could thus be evolved products of arc-like magmatism, suggesting reestablishment of a normal subduction system in this area, as it has been proposed for the Early to Late Cretaceous tectonic setting in SE China (e.g., He and Xu, 2012; Meng et al., 2012; Zhu et al., 2014).

6. Concluding remarks

(1) Zircon LA-MC-ICPMS and ID-TIMS U–Pb dating results obtained in this study indicate that the Macao region was the locus of multistage magmatism during the Yanshanian orogeny. Granitic magmatism occurred within approximately 155 and 165 Ma, concentrated between 164.5 ± 0.6 Ma and 162.9 ± 0.7 Ma (Group I) and 156.6 ± 0.2 Ma and 155.5 ± 0.8 Ma (Group II). In addition, dacite dykes cutting granites were dated at 150.6 ± 0.6 Ma and <120 Ma.

(2) Differences in the type of K-feldspar, accessory phases, biotite and whole-rock chemistry and in the mineralogy and textures of the associated MMEs, suggest that the two age groups correspond to two distinct pulses of granitic magmatism rather than a continuum of comagmatic activity.

(3) Trace element compositions show that magmas of the two groups evolved in different ways, producing distinct REE evolutionary paths. While Group I magmas seem to have evolved by progressive enrichment in heavy REE relatively to light REE, magmas from Group II are marked by depletion of middle REE leading to progressively concave REE patterns.

(4) Inheritance patterns in the zircon U–Pb data suggest the presence of a population of antecrysts (165–180 Ma) crystallized from earlier magmatic pulses and a population of inherited zircons and/or xenocrysts from Precambrian to Phanerozoic sources incorporated into the magmas during melting and/or ascent/emplacement at crustal levels. The oldest inherited ages (2.4 Ga and possibly 2.9 Ga) suggest contribution of Proterozoic and possibly of late Archaean crustal sources for the Macao magmatism.

(5) The Macao Group II granites clearly indicate the occurrence on the Pearl River Delta region of a magmatic pulse between those at the origin of Lamma Suite (165–160 Ma) and the Kwai Chung Suite (148–146 Ma) in the neighboring Hong Kong region. In addition, REE ratios suggest that this pulse may only occur in Macao area, while Macao Group I granites show evolving trends of REE ratios similar to those of Jurassic granites outcropping in vast areas of the Cathaysia Block (SE China).

(6) Considering the existence in Macao of two proximal but distinct granitic pulses spanning for a time of ca. 9 Ma and separated by ca. 6 Ma, we suggest that the Macao granitic suite was incrementally assembled, a hypothesis also extendable to the neighboring Hong Kong region. Given the relatively short time span between the two pulses and the chemical similarity of the less evolved rocks, the observed differences in the evolutionary trends are probably the result of a change in magma evolution processes rather than in tectonic setting, which was dominantly extensional related to the foundering of the subducting paleo-Pacific plate under the Eurasian plate during the Middle to Upper Jurassic.

(7) Despite Early Yanshanian magmatism being predominant in Macao, the younger ages obtained for the dacite dykes indicate that the territory was affected, to a lesser degree, by Late Yashanian magmatism. The change in the type of magmatism in Macao from granitic to dacitic is likely to correspond to a change in the regional tectonic regime inducing a significant change in the magma genesis processes. The dacite dykes may testify the reestablishment of a normal subduction system in this area of SE China.

Acknowledgments

This research was supported by the Macao Science and Technology Development Fund (FDCT 043/2014/A1). We also

acknowledge the support of FCT (Portugal) through UID/GEO/50019/2013 to Instituto Dom Luiz, Universidade de Lisboa. We are very grateful to Varon Lou (Lou U. Tat) and Ricardo Borges for their important help during the field and lab work and to Pedro Rodrigues for skilled assistance during electron microprobe analyses. We thank the two anonymous reviewers for their thoughtful reviews and constructive comments that greatly improved the manuscript.

Appendix A. Supplementary data

Supplementary data to this article can be found online at https://doi.org/10.1016/j.gsf.2019.04.011.

References

Abdel-Rahman, A.F.M., 1994. Nature of biotites from alkaline, calc-alkaline, and peraluminous magmas. Journal of Petrology 35, 525–541. https://doi.org/10.1093/petrology/35.2.525.

Annen, C., 2011. Implications of incremental emplacement of magma bodies for magma differentiation, thermal aureole dimensions and plutonism-volcanism relationships. Tectonophysics 500, 3–10. https://doi.org/10.1016/j.tecto.2009.04.010.

Arndt, N.T., 2013. Formation and evolution of the continental crust. Geochemical Perspectives 2, 405–533. https://doi.org/10.7185/geochempersp.2.3.

Bachman, O., Charlier, B.L.A., Lowenstern, J.B., 2007. Zircon crytallization and recycling in the magma chamber of the rhyolitic Kos Plateau Tuff (Aegean arc). Geology 35, 73–76. https://doi.org/10.1130/G23151A.1.

Barboni, M., Schoene, B., Ovtcharova, M., Bussy, F., Schaltegger, U., Gerdes, A., 2013. Timing of incremental pluton construction and magmatic activity in a back-arc setting revealed by ID-TIMS U/Pb and Hf isotopes on complex zircon grains. Chemical Geology 342, 76–93. https://doi.org/10.1016/j.chemgeo.2012.12.011.

Bea, F., Montero, P., Ortega, M., 2006. A LA-ICP-MS evaluation of Zr reservoirs in common crustal rocks: implications for Zr and Hf geochemistry, and zircon-forming processes. The Canadian Mineralogist 44, 693–714. https://doi.org/10.2113/gscanmin.44.3.693.

Beckinsale, R.D., 1979. Granite magmatism in the tin belt of Southeast Asia. In: Atherton, M.P., Tarney, J. (Eds.), Origin of Granite Batholiths Geochemical Evidence. Shiva Publishing Limited, Orpington, pp. 34–44.

Bell, T.H., Johnson, S.E., 1989. The role of deformation partitioning in the deformation and recrystallization of plagioclase and K-feldspar in the Woodroffe Thrust mylonite zone, central Australia. Journal of Metamorphic Geology 7, 151–168.

Bignell, J.D., Snelling, N.J., 1977. The geochronology of Malayan granites. In: Overseas Geology and Mineral Resources, vol. 47. H.M. Stationery Office, London, pp. 1–72.

Blasi, A., Brajkovic, A., de Pol Blasi, C., 1984. Dry-heating conversion of low microcline to high sanidine via a one-step disordering process. Bulletin de Mineralogie 107, 423–435.

Bónová, K., Broska, I., Petrík, I., 2010. Biotite from Čierna hora Mountains granitoids (Western Carpathians, Slovakia) and estimation of water contents in granitoid melts. Geologica Carpathica 61 (1), 3–17. https://doi.org/10.2478/v10096-009-0040-1.

Bruiyn, H. de, Van Der Westhuizen, W.A., Schoch, A.E., 1983. The estimation of FeO, F and H_2O^+ by regression in microprobe analyses of natural biotite. Journal of Trace and Microprobe Techniques 1, 399–413.

Campbell, S.D.G., Sewell, R.J., 1997. Structural control and tectonic setting of Mesozoic volcanism in Hong Kong. Journal of the Geological Society 154, 1039–1052. https://doi.org/10.1144/gsjgs.154.6.1039.

Campbell, S.D.G., Sewell, R.J., Davis, D.W., So, A.C.T., 2007. New U-Pb age and geochemical constraints on the stratigraphy and distribution of the Lantau Volcanic Group, Hong Kong. Journal of Asian Earth Sciences 31, 139–152. https://doi.org/10.1016/j.jseaes.2007.05.001.

Charlier, B.L.A., Wilson, C.J.N., Lowenstern, J.B., Blake, S., van Calsteren, P.W., Davidson, J.P., 2005. Magma generation at a large, hyperactive silicic volcano (Taupo, New Zealand) revealed by U-Th and U-Pb systematics in zircons. Journal of Petrology 46, 3–32. https://doi.org/10.1093/petrology/egh060.

Charvet, J., 2013. The Neoproterozoic-early Paleozoic tectonic evolution of the south China block: an overview. Journal of Asian Earth Sciences 74, 198–209. https://doi.org/10.1016/j.jseaes.2013.02.015.

Chen, C.H., Lee, C.Y., Lu, H.Y., Hsieh, P.S., 2008. Generation of Late Cretaceous silicic rocks in SE China: age, major element and numerical simulation constraints. Journal of Asian Earth Sciences 31, 479–498. https://doi.org/10.1016/j.jseaes.2007.08.002.

Chen, J.Y., Yang, J.H., Ji, W.Q., 2017. Ages and petrogenesis of Jurassic and Cretaceous intrusive rocks in the Matsu Islands: implications for lower crust modification beneath southeastern China. Journal of Asian Earth Sciences 150, 14–24. https://doi.org/10.1016/j.jseaes.2017.10.004.

Chen, T.G., 1987. Basic features of the Lianhuashan Fault zone in the Hong Kong and Shenzhen areas. Journal of Guangdong Geology 2, 57–68.

Chen, Y.W., Bi, X.W., Hu, R.Z., Dong, S.H., 2012. Element geochemistry, mineralogy, geochronology and zircon Hf isotope of the Luxi and Xiazhuang granites in Guangdong province, China: implications for U mineralization. Lithos 150, 119–134. https://doi.org/10.1016/j.lithos.2012.06.025.

Cherniak, D.J., Hanchar, J.M., Watson, E.B., 1997. Rare-earth diffusion in zircon. Chemical Geology 134, 289–301. https://doi.org/10.1016/S0009-2541(96)00098-8.

Cobbing, J., 2000. The Geology and Mapping of Granite Batholiths. Springer Berlin Heidelberg, p. 147.

Coleman, D.S., Gray, W., Glazner, A.F., 2004. Rethinking the emplacement and evolution of zoned plutons: Geochronologic evidence for incremental assembly of the Tuolumne Intrusive Suite, California. Geology 32, 433–436. https://doi.org/10.1130/G20220.1.

Collins, L.G., 2000. Overlooked experimental evidence for K-replacements of plagioclase and origin of microcline in granite plutons. Myrmekite Electronic Journal 37, 1–9.

Davis, D.W., Sewell, R.J., Campbell, S.D.G., 1997. U-Pb dating of Mesozoic igneous rocks from Hong Kong. Journal of the Geological Society 154, 1067–1076. https://doi.org/10.1144/gsjgs.154.6.1067.

Davis, D.W., Williams, I.S., Krogh, T.E., 2003. Historical development of zircon geochronology Donald. Reviews in Mineralogy and Geochemistry 53, 145–181. https://doi.org/10.2113/0530145.

Deer, W.A., Howie, R.A., Zussman, J., 1992. An Introduction to the Rock-Forming Minerals, second ed. Longmans, London, p. 696.

Ding, Y.Z., Lai, K.W., 1997. Neotectonic fault activity in Hong Kong : evidence from seismic events and thermoluminescence dating of fault gouge Neotectonic fault activity in Hong Kong : evidence from seismic events and thermoluminescence dating of fault gouge. Journal of the Geological Society 154, 1001–1007. https://doi.org/10.1144/gsjgs.154.6.1001.

Esmaeily, D., Maghdour-Mashhour, R., Shabani, T., Ali, A., 2013. Chemical characteristics of biotite from Boroujerd granitoid complex (middle Jurassic), western Iran. Geopersia 3, 69–78.

Foster, M.D., 1960. Interpretation of the composition of Trioctahedral micas interpretation of the composition of Trioctahedral micas. Geological Survey Professional Paper 354–B, 11–49.

Frazer, R.E., Coleman, D.S., Mills, R.D., 2014. Zircon U-Pb geochronology of the Mount Givens Granodiorite: Implications for the genesis of large volumes of eruptible magma. Journal of Geophysical Research-Solid Earth 119, 2907–2924. https://doi.org/10.1002/2013JB010716.Received.

Gillot, P.Y., Hildenbrand, A., Lefèvre, J.C., Albore Livadie, C., 2006. The K/Ar dating method: principle, analytical techniques, and application to Holocene volcanic eruptions in Southern Italy. Acta Vulcanologica 18, 55–66.

Glazner, A.F., Bartley, J.M., Coleman, D.S., Walt, G., Ryan, Z.T., 2004. Are plutons assembled over millions of years by amalgamation from small magma chambers? Geological Society of America Today 5173, 4–10. https://doi.org/10.1130/1052-5173(2004)014<0004.

Guo, C., Chen, Y., Zeng, Z., Lou, F., 2012. Petrogenesis of the Xihuashan granites in southeastern China: constraints from geochemistry and in-situ analyses of zircon U-Pb-Hf-O isotopes. Lithos 148, 209–227. https://doi.org/10.1016/j.lithos.2012.06.014.

Hanchat, J.M., Miller, C.F., 1993. Zircon zonation patterns as revealed by cathodoluminescence and backscattered electron images : implications for interpretation of complex crustal histories. Chemical Geology 110, 1–13.

Harley, S.L., Kelly, N.M., 2007. Zircon - Tiny but timely. Elements 3, 13–18.

He, Z.Y., Xu, X.S., 2012. Petrogenesis of the Late Yanshanian mantle-derived intrusions in southeastern China: response to the geodynamics of paleo-Pacific plate subduction. Chemical Geology 328, 208–221. https://doi.org/10.1016/j.chemgeo.2011.09.014.

He, Z.Y., Xu, X.S., Niu, Y., 2010. Petrogenesis and tectonic significance of a Mesozoic granite-syenite-gabbro association from inland South China. Lithos 119, 621–641. https://doi.org/10.1016/j.lithos.2010.08.016.

Horvat, M., Tibljas, D., Buda, G., Lovas, G., 2011. X-ray study of potassium feldspars from different granitoid types and gneisses of Papuk Mt. (Slavonia, Croatia). Geologia Croatica 64 (2), 153–162.

Huang, H.-Q., Li, X.-H., Li, Z.-X., Li, W.-X., 2012. Intraplate crustal remelting as the genesis of Jurassic high-K granites in the coastal region of the Guangdong Province, SE China. Journal of Asian Earth Sciences 74, 280–302. https://doi.org/10.1016/j.jseaes.2012.09.009.

Huang, H.-Q., Li, X.-H., Li, Z.-X., Li, W.-X., 2015. Formation of the Jurassic south China large granitic province: insights from the genesis of the Jiufeng pluton. Chemical Geology 401, 43–58. https://doi.org/10.1016/j.chemgeo.2015.02.019.

Huang, Y.K., Zhang, K., 1990. Some characteristics of neotectonic movements in the Lianhuashan Fault zone, Guangdong. Journal of South Chinese Seismology 10, 25–34.

Hürlimann, N., Müntener, O., Ulmer, P., Nandedkar, R., Chiaradia, M., Ovtcharova, M., 2016. Primary magmas in continental arcs and their differentiated products: petrology of a post-plutonic dyke suite in the Tertiary Adamello Batholith (Alps). Journal of Petrology 57, 495–534. https://doi.org/10.1093/petrology/egw016.

Irber, W., 1999. The lanthanide tetrad effect and its correlation with K/Rb, Eu/Eu*, Sr/Eu, Y/Ho, and Zr/Hf of evolving peraluminous granite suites. Geochimica et Cosmochimica Acta 63, 489–508. https://doi.org/10.1016/S0016-7037(99)00027-7.

Jackson, S.E., Pearson, N.J., Griffin, W.L., Belousova, E.A., 2004. The application of laser ablation-inductively coupled plasma-mass spectrometry to in situ U-Pb

zircon geochronology. Chemical Geology 211, 47–69. https://doi.org/10.1016/j.chemgeo.2004.06.017.
Jaffey, A.H., Flynn, K.F., Glendenin, L.E., Bentley, W.C., Essling, A.M., 1971. Precision measurement of half-lives and specific activities of ^{235}U and ^{238}U. Physical Review 4, 1889–1906. https://doi.org/10.1103/PhysRevC.4.1889.
Jiang, H., Jiang, S.-Y., Li, W.-Q., Zhao, K.D., Peng, N.-J., 2018. Highly fractionated Jurassic I-type granites and related tungsten mineralization in the Shirenzhang deposit, northern Guangdong, South China: evidence from cassiterite and zircon U-Pb ages, geochemistry and Sr-Nd-Pb-Hf isotopes. Lithos 312–313, 186–203. https://doi.org/10.1016/j.lithos.2018.04.030.
Jiang, Y.-H., Jiang, S.-Y., Dai, B.-Z., Liao, S.-Y., Zhao, K.-D., Ling, H.-F., 2009. Middle to late Jurassic felsic and mafic magmatism in southern Hunan province, southeast China: implications for a continental arc to rifting. Lithos 107, 185–204. https://doi.org/10.1016/j.lithos.2008.10.006.
Jiang, Y.-H., Wang, G.-C., Liu, Z., Ni, C.-Y., Qing, L., Zhang, Q., 2015. Repeated slab advance–retreat of the Palaeo-Pacific plate underneath SE China. International Geology Review 57, 472–491. https://doi.org/10.1080/00206814.2015.1017775.
Jiang, Y.-H., Zhu, S.-Q., 2017. Petrogenesis of the Late Jurassic peraluminous biotite granites and muscovite-bearing granites in SE China: geochronological, elemental and Sr–Nd–O–Hf isotopic constraints. Contributions to Mineralogy and Petrology 172, 101. https://doi.org/10.1007/s00410-017-1422-5.
Keay, S., Steele, D., Compston, W., 1999. Identifying granite sources by SHRIMP U-Pb zircon geochronology: an application to the Lachlan foldbelt. Contributions to Mineralogy and Petrology 137, 323–341. https://doi.org/10.1007/s004100050553.
Kelemen, P.B., Hanghøj, K., 2003. One view of the geochemistry of subduction-related magmatic arcs, with an emphasis on primitive Andesite and lower crust. In: Holland, H.D., Turekian, K.K. (Eds.), Treatise on Geochemistry. Elsevier, New York, pp. 593–659.
Keller, C.B., Schoene, B., Samperton, K.M., 2018. A stochastic sampling approach to zircon eruption age interpretation. Geochemical Perspectives Letters 8, 31–35. https://doi.org/10.7185/geochemlet.1826.
Kemp, A.I.S., Hawkesworth, C.J., 2003. Granitic perspectives on the generation and Secular evolution of the continental crust. In: Rudnick, R.L. (Ed.), The Crust, Treatise on Geochemistry, vol. 3. Elsevier, Amsterdan, pp. 350–410. https://doi.org/10.1016/B0-08-043751-6/03027-9.
Krogh, T., 1973. A low-contamination method for hydrothermal decomposition of zircon and extraction of U and Pb for isotopic age determinations. Geochimica et Cosmochimica Acta 37, 485–494. https://doi.org/10.1016/0016-7037(73)90213-5.
Lapierre, H., Jahn, B.M., Charvet, J., Yu, Y.W., 1997. Mesozoic felsic arc magmatism and continental olivine tholeiites in Zhejiang Province and their relationship with the tectonic activity in southeastern China. Tectonophysics 274, 321–338. https://doi.org/10.1016/S0040-1951(97)00009-7.
Lee, J.K.W., 2014. Ar–Ar and K–Ar dating. In: Jack Rink, W., Thompson, Jeroen W. (Eds.), Encyclopedia of Scientific Dating Methods. Springer, Netherlands, pp. 1–27. https://doi.org/10.1007/978-94-007-6326-5.
Lee, J.K.W., Williams, I.S., Ellis, D.J., 1997. Pb, U and Th diffusion in natural zircon. Nature 390, 159–162. https://doi.org/10.1038/36554.
Li, B., Jiang, S.-Y., Zhang, Q., Zhao, H.-X., Zhao, K.-D., 2015. Cretaceous crust–mantle interaction and tectonic evolution of Cathaysia Block in South China: evidence from pulsed mafic rocks and related magmatism. Tectonophysics 661, 136–155. https://doi.org/10.1016/j.tecto.2015.08.032.
Li, X.-H., 1997. Timing of the Chathaysia block formation: constraints from SHRIMP U-Pb zircon geochronology. Episodes 20, 188–192.
Li, X.-H., Chen, Z., Liu, D., Li, W.-X., 2003. Jurassic gabbro-granite-syenite suites from southern Jiangxi province, SE China. Age, origin, and tectonic significance. International Geology Review 45, 898–921. https://doi.org/10.2747/0020-6814.45.10.898.
Li, X.-H., Chung, S.-L., Zhou, H., Lo, C.-H., Liu, Y., Chen, C.-H., 2004. Jurassic intraplate magmatism in southern Hunan-eastern Guangxi: ^{40}Ar/^{39}Ar dating, geochemistry, Sr-Nd isotopes and implications for the tectonic evolution of SE China. Geological Society London Special Publications 226 (1), 193–215. https://doi.org/10.1144/GSL.SP.2004.226.01.11.
Li, X.-H., Li, Z., Li, W.-X., 2014. Detrital zircon U – Pb age and Hf isotope constrains on the generation and reworking of Precambrian continental crust in the Cathaysia Block, South China : a synthesis. Gondwana Research 25, 1202–1215. https://doi.org/10.1016/j.gr.2014.01.003.
Li, X.-H., Li, Z.X., Li, W.-X., Liu, Y., Yuan, C., Wei, G., Qi, C., 2007. U-Pb zircon, geochemical and Sr-Nd-Hf isotopic constraints on age and origin of Jurassic I- and A-type granites from central Guangdong, SE China: a major igneous event in response to foundering of a subducted flat-slab. Lithos 96, 186–204. https://doi.org/10.1016/j.lithos.2006.09.018.
Li, X.-H., Sun, M., Wei, G.J., Liu, Y., Lee, C.Y., Malpas, J., 2000. Geochemical and Sm-Nd isotopic study of amphibolites in the Cathaysia Block, southeastern China: evidence for an extremely depleted mantle in the Paleoproterozoic. Precambrian Research 102, 251–262. https://doi.org/10.1016/S0301-9268(00)00067-X.
Li, X.Y., Zheng, J.P., Xiong, Q., Zhou, X., Xiang, L., 2018. Triassic rejuvenation of unexposed Archean-Paleoproterozoic deep crust beneath the western Cathaysia block, South China. Tectonophysics 724–725, 65–79. https://doi.org/10.1016/j.tecto.2018.01.005.
Li, Z.X., Li, X.-H., Zhou, H., Kinny, P.D., 2002. Grenvillian continental collision in south China : new SHRIMP U-Pb zircon results and implications for the configuration of Rodinia. Geology 30, 163–166.
Li, Z.X., Li, X.-H., 2007. Formation of the 1300-km-wide intracontinental orogen and postorogenic magmatic province in Mesozoic South China: a flat-slab subduction model. Geology 35, 179–182. https://doi.org/10.1130/G23193A.1.
Liu, Q., Yu, J., Reilly, S.Y.O., Zhou, M., Griffin, W.L., Wang, L., Cui, X., 2014. Origin and geological significance of Paleoproterozoic granites in the northeastern Cathaysia block, south China. Precambrian Research 248, 72–95. https://doi.org/10.1016/j.precamres.2014.04.001.
Liu, Y., Gao, S., Hu, Z., Gao, C., Zong, K., Wang, D., 2009. Continental and oceanic crust recycling-induced melt-peridotite interactions in the Trans-North China Orogen: U-Pb dating, Hf isotopes and trace elements in zircons from mantle xenoliths. Journal of Petrology 51, 537–571. https://doi.org/10.1093/petrology/egp082.
Ludwig, K.R., 1998. On the treatment of concordant uranium-lead ages. Geochimica et Cosmochimica Acta 62, 665–676. https://doi.org/10.1016/S0016-7037(98)00059-3.
Ludwig, K.R., 2012. User's Manual for Isoplot 3.75, a Geochronological Toolkit for Microsoft Excel, vol. 5. Berkeley Geochronology Center Special Publication, pp. 1–72.
Mattinson, J.M., 2005. Zircon U-Pb chemical abrasion ("CA-TIMS") method: combined annealing and multi-step partial dissolution analysis for improved precision and accuracy of zircon ages. Chemical Geology 220, 47–66. https://doi.org/10.1016/j.chemgeo.2005.03.011.
Matzel, J.E.P., Bowring, S.A., Miller, R.B., 2006. Time scales of pluton construction at differing crustal levels: examples from the Mount Stuart and Tenpeak intrusions, North Cascades, Washington. Bulletin of the Geological Society of America 118, 1412–1430. https://doi.org/10.1130/B25923.1.
McDonough, W.F., Sun, S. -S., 1995. The composition of the Earth. Chemical Geology 120, 223–253. https://doi.org/10.1016/0009-2541(94)00140-4.
Memeti, V., Paterson, S., Matzel, J., Mundil, R., Okaya, D., 2010. Magmatic lobes as "snapshots" of magma chamber growth and evolution in large, composite batholiths: an example from the Tuolumne intrusion, Sierra Nevada, California. Bulletin of the Geological Society of America 122, 1912–1931. https://doi.org/10.1130/B30004.1.
Menand, T., Annen, C., Blanquat, M. de Saint, 2015. Rates of magma transfer in the crust: insights into magma reservoir recharge and pluton growth. Geology 43, 199–202. https://doi.org/10.1130/G36224.1.
Meng, L., Li, Z.X., Chen, H., Li, X.H., Wang, X.C., 2012. Geochronological and geochemical results from Mesozoic basalts in southern South China Block support the flat-slab subduction model. Lithos 132–133, 127–140. https://doi.org/10.1016/j.lithos.2011.11.022.
Miller, C.F., McDowell, S.M., Mapes, R.W., 2003. Hot and cold granites: implications of zircon saturation temperatures and preservation of inheritance. Geology 31, 529–532. https://doi.org/10.1130/0091-7613(2003)031<0529:HACGIO>2.0.CO;2.
Miller, J.S., Matzel, J.E.P., Miller, C.F., Burgess, S.D., Miller, R.B., 2007. Zircon growth and recycling during the assembly of large, composite arc plutons. Journal of Volcanology and Geothermal Research 167, 282–299. https://doi.org/10.1016/j.jvolgeores.2007.04.019.
Nachit, H., Ibhi, A., Abia, E.H., Ben Ohoud, M., 2005. Discrimination between primary magmatic biotites, reequilibrated biotites and neoformed biotites. Comptes Rendus Geoscience 337, 1415–1420. https://doi.org/10.1016/j.crte.2005.09.002.
Nachit, H., Razafimahefa, N., Stussi, J.M., Carron, J.P., 1985. Composition chimique des biotites et typologie magmatique des granites. C.R. Acad. Sci. Paris, Sér. II 301, 813–818.
Qiu, Y.M., Gao, S., McNaughton, N.J., Groves, D.I., Ling, W., 2000. First evidence of >3.2 Ga continental crust in the Yangtze craton of south China and its implications for Archean crustal evolution and Phanerozoic tectonics. Geology 28, 11–14. https://doi.org/10.1130/00917613(2000)028<0011:FEOGCC>2.3.CO;2.
Qiu, Z., et al., 2017. Highly fractionated Early Cretaceous I-type granites and related Sn polymetallic mineralization in the Jinkeng deposit, eastern Guangdong, SE China: constraints from geochronology, geochemistry, and Hf isotopes. Ore Geology Reviews 88, 718–738. https://doi.org/10.1016/j.oregeorev.2016.10.008.
Qiu, Z., Yan, Q., Li, S., Wang, H., Tong, L., Zhang, R., Wei, X., Li, P., Wang, L., Bu, A., Yan, L., 2016. Highly fractionated Early Cretaceous I-type granites and related Sn polymetallic mineralization in the Jinkeng deposit, eastern Guangdong, SE China: constraints from geochronology, geochemistry, and Hf isotopes. Ore Geology Reviews 88, 718–738. https://doi.org/10.1016/j.oregeorev.2016.10.008.
Ribeiro, M.L., Ramos, J.M.F., Pereira, E., Dias, R.P., 1992. Notícia Explicativa da Carta Geológica de Macau na escala 1/5000. Serviços Geológicos de Portugal (in Portuguese).
Ribeiro, M.L., Ramos, J.M.F., Pereira, E., Dias, R.P., 2010. Macau, Evolução do Conhecimento Geológico. Geologia das Ex-Colónias da Ásia e Oceânia. Macau 3, 259–266 (in Portuguese).
Rieder, M., 1999. Nomenclature of the micas. Mineralogical Magazine 63, 267–279. https://doi.org/10.1180/minmag.1999.063.2.13.
Roberts, N.M.W., Spencer, C.J., 2015. The zircon archive of continent formation through time. Geological Society London Special Publications 389, 197–225. https://doi.org/10.1144/SP389.14.
Rubatto, D., Gebauer, D., 2000. Use of cathodoluminescence for U-Pb zircon dating by ion microprobe: some examples from the western Alps Chapter. In: Pagel, M., Barbin, V., Blanc, P., Ohnenstetter, D. (Eds.), Cathodoluminescence in Geosciences. Springer Berlin Heidelberg, pp. 373–400. https://doi.org/10.1007/978-3-662-04086-7.
Rudnick, R.L., Gao, S., 2003. Composition of the continental crust. In: Holland, H.D., Turekian, K.K. (Eds.), The Crust, Treatise on Geochemistry, vol. 3. Elsevier-Pergamon, Oxford, pp. 1–64.

Sambridge, M.S., Compston, W., 1994. Mixture modeling of multi-component data sets with application to ion-probe zircon ages. Earth and Planetary Science Letters 128, 373–390. https://doi.org/10.1016/0012-821X(94)90157-0.
Scherer, E.E., Whitehouse, M.J., Münker, C., 2007. Zircon as a monitor of crustal growth. Elements 3, 19–24. https://doi.org/10.2113/gselements.3.1.19.
Schoene, B., Schaltegger, U., Brack, P., Latkoczy, C., Stracke, A., Günther, D., 2012. Rates of magma differentiation and emplacement in a ballooning pluton recorded by U-Pb TIMS-TEA, Adamello batholith, Italy. Earth and Planetary Science Letters 355–356, 162–173. https://doi.org/10.1016/j.epsl.2012.08.019.
Sewell, R.J., Campbell, S.D.G., 1997. Geochemistry of coeval Mesozoic plutonic and volcanic suites in Hong Kong. Journal of the Geological Society 154, 1053–1066. https://doi.org/10.1144/gsjgs.154.6.1053.
Sewell, R.J., Darbyshire, D.P.F., Langford, R.L., Strange, P.J., 1992. Geochemistry and Rb-Sr geochronology of Mesozoic granites from Hong Kong. Earth and Environmental Science Transactions of the Royal Society of Edinburgh 83, 269–280. https://doi.org/10.1017/S0263593300007951.
Sewell, R.J., Davis, D.W., Campbell, S.D.G., 2012. High precision U-Pb zircon ages for Mesozoic igneous rocks from Hong Kong. Journal of Asian Earth Sciences 43, 164–175. https://doi.org/10.1016/j.jseaes.2011.09.007.
Sewell, R.J., Carter, A., Rittner, M., 2016. Middle Jurassic collision of an exotic microcontinental fragment: Implications for magmatism across the Southeast China continental margin. Gondwana Research 38, 304–312. https://doi.org/10.1016/j.gr.2016.01.005.
Smith, J.V., Brown, W.L., 1974. Feldspar Minerals 1. Crystal Structures, Physical, Chemical and Microtextural Properties. Springer Berlin Heidelberg, p. 828.
Speer, J.A., 1984. Micas in igneous rocks. Reviews in Mineralogy and Geochemistry 13 (1), 299–356.
Tang, D.L.K., Seward, D., Wilson, C.J.N., Sewell, R.J., Carter, A., Paul, B.T., 2014. Thermotectonic history of SE China since the Late Mesozoic: insights from detailed thermochronological studies of Hong Kong. Journal of the Geological Society 171, 591–604. https://doi.org/10.1144/jgs2014-009.
Vernon, R.H., Paterson, S.R., 2002. Igneous origin of K-feldspar megacrysts in deformed granite of the Papoose Flat Pluton, California, USA. Electonic Geosciences 7, 31–39. https://doi.org/10.1007/s10069-002-0005-3.
Wang, Y., Fan, W., Cawood, P.A., Li, S., 2008. Sr-Nd-Pb isotopic constraints on multiple mantle domains for Mesozoic mafic rocks beneath the South China Block hinterland. Lithos 106, 297–308. https://doi.org/10.1016/j.lithos.2008.07.019.
Wang, Y., Fan, W., Zhang, G., Zhang, Y., 2013. Phanerozoic tectonics of the south China block: key observations and controversies. Gondwana Research 23, 1273–1305. https://doi.org/10.1016/j.gr.2012.02.019.
Watson, E.B., Harrison, T.M., 1983. Zircon saturation revisited: temperature and composition effects in a variety of crustal magma types. Earth and Planetary Science Letters 64, 295–304. https://doi.org/10.1016/0012-821X(83)90211-X.
Wiedenbeck, M., Allé, P., Corfu, F., Griffin, W.L., Meier, M., Oberli, F., Quadt, A.V.O.N., Roddick, J.C., Spiegel, W., 1995. Three natural zircon standards for U-Th-Pb, Lu-Hf, trace element and REE analyses. Geostandards Newsletter 19, 1–23. https://doi.org/10.1111/j.1751-908X.1995.tb00147.x.
Wones, D.R., Eugster, H.P., 1965. Stability of biotite: experiment, theory, and application. American Mineralogist 50, 1228–1272.
Xia, S., Zhao, D., 2014. Late Mesozoic magmatic plumbing system in the onshore-offshore area of Hong Kong: insight from 3-D active-source seismic tomography. Journal of Asian Earth Sciences 96, 46–58. https://doi.org/10.1016/j.jseaes.2014.08.038.
Xia, X., Sun, M., Geng, H., Sun, Y., Wang, Y., Zhao, G., 2011. Quasi-simultaneous determination of U-Pb and Hf isotope compositions of zircon by excimer laser-ablation multiple-collector ICPMS. Journal of Analytical Atomic Spectrometry 26, 1868–1871. https://doi.org/10.1039/c1ja10116a.
Xu, B., Jiang, S.Y., Wang, R., Ma, L., Zhao, K. dong, Yan, X., 2015. Late Cretaceous granites from the giant Dulong Sn-polymetallic ore district in Yunnan Province, South China. Geochronology, geochemistry, mineral chemistry and Nd-Hf isotopic compositions. Lithos 218–219, 54–72. https://doi.org/10.1016/j.lithos.2015.01.004.
Xu, X., Lu, W., He, Z., 2007. Age and generation of Fogang granite batholith and Wushi diorite-hornblende gabbro body. Science in China Series D (Earth Sciences) 50, 209–220. https://doi.org/10.1007/s11430-007-2068-3.
Yan, Q.H., Li, S.S., Qiu, Z.W., Wang, H., Wei, X.P., Pei-Li, Dong, R., Zhang, X.Y., 2017. Geochronology, geochemistry and Sr–Nd–Hf–S–Pb isotopes of the Early Cretaceous Taoxihu Sn deposit and related granitoids, SE China. Ore Geology Reviews 89, 350–368. https://doi.org/10.1016/j.oregeorev.2017.05.026.
Ye, M., Li, X., Li, W., Liu, Y., Li, Z., 2007. SHRIMP zircon U–Pb geochronological and whole-rock geochemical evidence for an early Neoproterozoic Sibaoan magmatic arc along the southeastern margin of the Yangtze Block. Gondwana Research 12, 144–156. https://doi.org/10.1016/j.gr.2006.09.001.
Yu, J., Reilly, S.Y.O., Zhou, M., Griffin, W.L., Wang, L., 2012. U–Pb geochronology and Hf–Nd isotopic geochemistry of the Badu complex, southeastern China : implications for the precambrian crustal evolution and paleogeography of the Cathaysia block. Precambrian Research 222–223, 424–449. https://doi.org/10.1016/j.precamres.2011.07.014.
Zaraisky, G.P., Aksyuk, A.M., Devyatova, V.N., Udoratina, O.V., Chevychelov, V.Y., 2009. The Zr/Hf ratio as a fractionation indicator of rare-metal granites. Petrology 17, 25–45. https://doi.org/10.1134/S0869591109010020.
Zhang, S.B., Zheng, Y.F., 2013. Formation and evolution of Precambrian continental lithosphere in South China. Gondwana Research 23, 1241–1260. https://doi.org/10.1016/j.gr.2012.09.005.
Zhang, Y., Yang, J.-H., Chen, J.-Y., Wang, H., Xi-ang, Y.-X., 2017. Petrogenesis of Jurassic tungsten-bearing granites in the Nanling Range, South China: evidence from whole-rock geochemistry and zircon U–Pb and Hf–O isotopes. Lithos 278–281, 166–180. https://doi.org/10.1016/j.lithos.2017.01.018.
Zhang, Y., Yang, J.-H., Sun, J.-F., Zhang, J.-H., Chen, J.-Y., Li, X.-H., 2015. Petrogenesis of Jurassic fractionated I-type granites in Southeast China : constraints from whole-rock geochemical and zircon U–Pb and Hf–O isotopes petrogenesis of Jurassic fractionated I-type granites in Southeast China. Journal of Asian Earth Sciences 111, 268–283. https://doi.org/10.1016/j.jseaes.2015.07.009.
Zhao, J.-L., Qiu, J.-S., Liu, L., Wang, R.-Q., 2016. The Late Cretaceous I- and A-type granite association of southeast China: implications for the origin and evolution of post-collisional extensional magmatism, 240–243. Elsevier B.V., pp. 16–33. https://doi.org/10.1016/j.lithos.2015.10.018
Zhao, X., Liu, K., Yu, M., Jiang, Y., Mao, J., Zhou, X., Yu, S., 2015. Early Cretaceous I-type granites in the southwest Fujian Province: new constraints on the late Mesozoic tectonic evolution of southeast China. Island Arc 24, 359–378. https://doi.org/10.1111/iar.12119.
Zheng, J.P., Griffin, W.L., Li, L.S., O'Reilly, S.Y., Pearson, N.J., Tang, H.Y., Liu, G.L., Zhao, J.H., Yu, C.M., Su, Y.P., 2011. Highly evolved Archean basement beneath the western Cathaysia block, south China. Geochimica et Cosmochimica Acta 75, 242–255. https://doi.org/10.1016/j.gca.2010.09.035.
Zheng, W., Mao, J., Zhao, H., Ouyang, H., Zhao, C., Yu, X., 2017a. Geochemistry, Sr–Nd–Pb–Hf isotopes systematics and geochronological constrains on petrogenesis of the Xishan A-type granite and associated W–Sn mineralization in Guangdong Province, South China. Ore Geology Reviews 88, 739–752. https://doi.org/10.1016/j.oregeorev.2016.12.021.
Zheng, W., Mao, J., Zhao, H., Zhao, C., Yu, X., 2017b. Two Late Cretaceous A-type granites related to the Yingwuling W–Sn polymetallic mineralization in Guangdong province, South China: implications for petrogenesis, geodynamic setting, and mineralization. Lithos 274–275, 106–122. https://doi.org/10.1016/j.lithos.2017.01.002.
Zhou, X.M., Li, W.X., 2000. Origin of late mesozoic igneous rocks in Southeastern China: Implications for lithosphere subduction and underplating of mafic magmas. Tectonophysics 326, 269–287. https://doi.org/10.1016/S0040-1951(00)00120-7.
Zhou, X.-M., Sun, T., Shen, W.-Z., Shu, L.-S., Niu, Y.L., 2006. Petrogenesis of Mesozoic granitoids and volcanic rocks in south China : a response to tectonic evolution. Episodes 29, 26–33.
Zhou, Z., Ma, C., Xie, C., Wang, L., Liu, Y., Liu, W., 2016. Genesis of highly fractionated I-type granites from Fengshun complex: implications to tectonic evolutions of South China. Journal of Earth Sciences 27, 444–460. https://doi.org/10.1007/s12583-016-0677-3.
Zheng, J., Griffin, W.L., O'Reilly, S.Y., Pearson, N., Pan, Y., 2006. Widespread Archean basement beneath the Yangtze craton. Geology 34 (2006), 417–420. https://doi.org/10.1130/G22282.1.
Zhu, K., Li, Z., Xu, X., Petrology, A., 2014. A Mesozoic Andean-type orogenic cycle in southeastern China as recorded by granitoid evolution. American Journal of Science 314, 187–234. https://doi.org/10.2475/01.2014.06.